8-20-2008

High-Resolution Chandra X-Ray Imaging And Spectroscopy Of The Sigma Orionis Cluster

S. L. Skinner

K. R. Sokal

David H. Cohen
Swarthmore College, dcohen1@swarthmore.edu

M. Gagné

S. P. Owocki

See next page for additional authors

Recommended Citation

S. L. Skinner, K. R. Sokal, David H. Cohen, M. Gagné, S. P. Owocki, and R. H.D. Townsend. (2008). "High-Resolution Chandra X-Ray Imaging And Spectroscopy Of The Sigma Orionis Cluster". *Astrophysical Journal*. Volume 683, Issue 2. 796-812. DOI: 10.1086/589917
https://works.swarthmore.edu/fac-physics/29

The Astrophysical Journal, 683:796–812, 2008 August 20

HIGH-RESOLUTION *CHANDRA* X-RAY IMAGING AND SPECTROSCOPY OF THE σ ORIONIS CLUSTER

Stephen L. Skinner and Kimberly R. Sokal
CASA, University of Colorado, Boulder, CO 80309-0389

David H. Cohen
Department of Physics and Astronomy, Swarthmore College, Swarthmore, PA 19081

Marc Gagné
Department of Geology and Astronomy, West Chester University, West Chester, PA 19383-2130

and

Stanley P. Owocki and Richard D. Townsend
Bartol Research Institute, University of Delaware, Newark, DE 19716
Received 2008 March 2; accepted 2008 May 6

ABSTRACT

We present results of a 90 ks *Chandra* X-ray observation of the young σ Orionis cluster (age $\sim$ 3 Myr) obtained with the HETGS. We use the high-resolution grating spectrum and moderate-resolution CCD spectrum of the massive central star σ Ori AB (O9.5 V + B0.5 V) to test wind shock theories of X-ray emission and also analyze the high spatial resolution zero-order ACIS-S image of the central cluster region. *Chandra* detected 42 X-ray sources on the primary CCD (ACIS-S3). All but five have near-IR or optical counterparts and about one-fourth are variable. Notable high-mass stellar detections are σ Ori AB, the magnetic B star σ Ori E, and the B5 V binary HD 37525. Most of the other detections have properties consistent with lower mass K- or M-type stars. We present the first X-ray spectrum of the unusual infrared source IRS 1, located $\approx 3''$ north of σ Ori AB. Its X-ray properties and elongated mid-IR morphology suggest that it is an embedded low-mass T Tauri star whose disk/envelope is being photoevaporated by σ Ori AB. We focus on the radiative wind shock interpretation of the soft luminous X-ray emission from σ Ori AB, but also consider possible alternatives including magnetically confined wind shocks and colliding wind shocks. Its emission lines show no significant asymmetries or centroid shifts and are moderately broadened to HWHM $\approx$ 264 km s^{-1}, or one-fourth the terminal wind speed. Forbidden lines in He-like ions are formally undetected, implying strong UV suppression. The Mg XI triplet forms in the wind acceleration zone within one stellar radius above the surface. These X-ray properties are consistent in several respects with the predictions of radiative wind shock theory for an optically thin wind, but explaining the narrow line widths presents a challenge to the theory.

Subject headings: open clusters and associations: individual (σ Orionis) — stars: formation — stars: individual (σ Orionis AB) — stars: pre–main-sequence — X-rays: stars

1. INTRODUCTION

Sensitive X-ray grating observations of massive OB stars with *Chandra* and *XMM-Newton* during the past several years have provided a wealth of new data that are improving our understanding of the physical processes that produce their X-ray emission. Luminous OB stars are not expected to have the outer convection zones needed to sustain internally generated magnetic fields and solar-like (coronal) X-ray emission. Thus, their X-ray emission has generally been attributed to wind shocks.

Theoretical models have attempted to explain the X-ray emission of *single* massive OB stars in terms of X-ray–emitting shocks distributed throughout their powerful winds that form as a result of line-driven flow instabilities (Lucy & White 1980; Lucy 1982; Feldmeier et al. 1997a; Owocki et al. 1988). The radiative wind shock emission is predicted to be soft ($kT \ll 1$ keV), in contrast to the harder emission ($kT \gtrsim 2$ keV) that has been detected in some massive colliding wind binaries and in a few OB stars with strong $\sim$kG magnetic fields whose winds are magnetically confined (§§ 3.4 and 3.7.2). X-ray grating observations provide crucial information on line shapes, widths, centroids, and fluxes needed to test wind shock models.

Grating observations of a limited sample of O- and early B-type stars have provided some support for the radiative wind shock picture. Perhaps the best support so far comes from the O4f star ζ Pup, which has a high mass-loss rate $\log \dot{M} \sim -5.3\ M_\odot\ \mathrm{yr}^{-1}$ (Pauldrach et al. 1994). Its X-ray emission lines are asymmetric with blueshifted centroids and are quite broad with half-width half-maximum values HWHM $\sim$ 900 km s^{-1}, equivalent to $\approx$40% of the terminal wind speed (Cassinelli et al. 2001; Kahn et al. 2001; Kramer et al. 2003). An analysis of a *Chandra* grating spectrum of the O9 supergiant ζ Ori by Cohen et al. (2006) also revealed broad blueshifted asymmetric emission lines, a different conclusion than was reached by Waldron & Cassinelli (2001). The blueshifted asymmetry is predicted by radiative wind shock models of optically thick winds where the redward part of the line is attenuated from receding wind material on the far side of the star (Owocki & Cohen 2001).

For late O-type and early B-type stars with lower mass-loss rates than O supergiants, clear confirmation of radiative wind shock theory has been more difficult to obtain. Grating spectra of the Orion belt eclipsing binary system δ Ori (O9.5 II + B0.5 III; $\log \dot{M} \sim -6.\ M_\odot\ \mathrm{yr}^{-1}$; Miller et al. 2002) reveal cool plasma at $kT \sim 0.3$ keV and symmetric unshifted emission lines with HWHM $\sim$ 430 km s^{-1}, or $\approx$22% of the terminal wind speed. The dominant cool plasma is compatible with a shock origin, and symmetric unshifted lines are predicted by radiative wind shock simulations for an optically thin wind (Macfarlane et al.

1991; Owocki & Cohen 2001). However, Miller et al. (2002) raised some questions about the surprising narrowness and symmetry of the lines in the framework of radiative wind shock models. An even more extreme case is the early B giant β Cru (B0.5 III; $\log \dot{M} \sim -8.$ $M_\odot$ yr^{-1}; Cohen et al. 2008). It also has a low plasma temperature and symmetric unshifted lines that are quite narrow (HWHM ~ 150 km s^{-1}). Cohen et al. (2008) concluded that the narrow lines were difficult to understand in the framework of radiative wind shock theory for fast winds.

Only a handful of X-ray grating observations of OB stars have been obtained, and observations of a broader sample of objects are needed to clarify how X-ray properties vary with spectral type, luminosity class, and mass-loss parameters. The Orion complex is particularly well suited to observational tests of X-ray emission models in massive young stars because of its relative proximity and large concentration of very young OB stars. It is the closest giant molecular cloud containing young massive stars. The density of young stars in Orion is high, and the deep *Chandra* observation of the Orion Nebula obtained in the COUP project detected more than 1400 X-ray sources (Getman et al. 2005). *Chandra*'s superb angular resolution is clearly an advantage in deep X-ray observations of Orion in order to avoid source misidentification.

A promising target for exploring X-ray production in young high-mass stars is σ Orionis AB (Table 1), the focus of this study. It is located in the Ori OB1b association and is quite young with an estimated age of 3 ± 2 Myr (Caballero 2007a and references therein; Caballero 2008). The *Hipparcos* distance is 352^{+166}_{-85} pc, which we adopt here. A slightly smaller value of 334^{+25}_{-22} pc was recently obtained by Caballero (2008), who also noted that $d \sim 385$ pc is possible if σ Ori AB is a triple system. For comparison, recent distance measurements of the Orion Nebula cluster (ONC) give 389^{+24}_{-21} pc (Sandstrom et al. 2007), 392^{+32}_{-32} pc (Jeffries 2007), 414 ± 7 pc (Menten et al. 2007), and 391^{+12}_{-9} pc (Mayne & Naylor 2008).

The pair σ Ori AB is a visual binary consisting of an O9.5 V primary and a B0.5 V companion separated by $0.25''$ (Mason et al. 1998) and is known to be a bright X-ray source (Berghöfer & Schmitt 1994; Berghöfer et al. 1996). The A and B components cannot be separated by existing X-ray telescopes. At a distance of 352 pc, the angular separation equates to a projected linear separation of 88 AU, or $2101 R_{\rm O\ star}$ (Table 1). The extinction toward σ Ori AB is low with $E(B-V) = 0.05-0.07$ (Table 1), thus minimizing interstellar absorption of any soft X-rays that might be produced in stellar wind shocks. In terms of wind strength, σ Ori A provides a good comparison with observations of other OB stars. Its wind is much weaker than the O4f star ζ Pup, and its mass-loss rate falls roughly in between that of the moderate wind source δ Ori and the weak wind source β Cru.

There is additional interest in σ Ori AB because it is surrounded by a cluster of several hundred young stars, originally discovered in *Röntgensatellit* (*ROSAT*) X-ray observations (Walter et al. 1997). *Spitzer* mid-IR observations have identified more than 300 cluster members, with a disk fraction of $\approx$35% in low-mass stars (Hernández et al. 2007). A similar disk fraction was found by Oliveira et al. (2006) from ground-based K- and L'-band images. A recent analysis of Tycho photometry by Mayne & Naylor (2008) gives a nominal cluster age of $\sim$3 Myr and a distance of 389^{+34}_{-24} pc. Some stars are still in the accretion phase, but the estimated accretion rates are low, with typical values $\dot{M}_{\rm acc} < 10^{-8}$ $M_\odot$ yr^{-1} (Gatti et al. 2008). This may have some effect on X-ray emission, which is of primary interest here, given that several studies suggest that the X-ray luminosities of accreting classical T Tauri stars are on average about a factor of $\sim$2 lower than their nonaccreting counterparts, the weak-lined T Tauri stars (Preibisch et al. 2005; Franciosini et al. 2006, hereafter FPS06; Telleschi et al. 2007).

TABLE 1
σ Ori AB Properties

Parameter	Value	References
Spectral type	O9.5 V + B0.5 V	1
Distance[a] (pc)	352^{+166}_{-85}	2
V (mag)	3.80–3.81	3, 4, 5
$E(B-V)$ (mag)	0.05–0.07[b]	3, 4, 5
$T_{\rm eff}$ (K)	33,000	6
R_* ($R_\odot$)	9	6
$\log \dot{M}$ ($M_\odot$ yr^{-1})	-7.1	6
v_∞ (km s^{-1})	1060	6
$\log (L_*/L_\odot)$	4.9	6
$\log L_{\rm wind}$[c] (ergs s^{-1})	34.4	6
$\log L_{\rm X}$ (ergs s^{-1})	31.5	7
$\log (L_{\rm X}/L_*)$	-7.0	7

Notes.—σ Ori A = HD 37468. $L_{\rm X}$ is the unabsorbed value in the 0.5–7 keV range.

[a] We adopt $d = 352$ pc in this work. A distance $d = 334^{+25}_{-22}$ pc was determined by Caballero (2008), who also noted that $d \sim 385$ pc is possible if the system is a triple.

[b] Adopting $A_V \approx 3E(B-V) = 0.15$–$0.21$ mag gives $N_{\rm H} = (3.3-4.7) \times 10^{20}$ cm^{-2} using the Gorenstein (1975) conversion.

[c] $L_{\rm wind} = \dot{M} v_\infty^2/2$.

References.—(1) Edwards 1976; (2) *Hipparcos* (Perryman et al. 1997); (3) Lee 1968; (4) Savage et al. 1985; (5) Vogt 1976; (6) Howarth & Prinja 1989; (7) this work (0.5–7 keV).

X-ray observations of the σ Ori region have also been obtained with *XMM-Newton*, and 174 X-ray sources were detected, 76 of which were identified with cluster members (Sanz-Forcada et al. 2004; FPS06). A 98 ks *Chandra* HRC-I observation (ObsID 2560) has also been acquired, detecting more than 140 X-ray sources (Wolk et al. 2006), including faint X-ray emission from the infrared source IRS 1 located just $3.3''$ north of σ Ori AB (van Loon & Oliveira 2003; Caballero 2007b).

We present results of a sensitive *Chandra* X-ray observation of the σ Ori cluster obtained with the High Energy Transmission Grating (HETG) and the ACIS-S detector. This observation provides higher spatial resolution than the previous *XMM-Newton* observation, but over a smaller field of view. The spatial resolution acquired here is comparable to that of the *Chandra* HRC-I observation, but the HETG/ACIS-S combination provides spectral information, whereas HRC-I does not. On the other hand, the HRC-I observation is more sensitive, covers a larger field of view, and gives superior image quality. Thus, the existing *Chandra* and *XMM-Newton* data sets are complementary.

Our primary objective was to obtain a high-resolution X-ray spectrum of σ Ori AB to test wind shock models of X-ray emission in massive stars. We focus on spectral properties of σ Ori AB but also analyze zeroth-order CCD images, spectra, and light curves of 41 other X-ray sources near σ Ori AB, including the magnetic helium-strong B2 Vpe star σ Ori E (HD 37479) and the unusual infrared source IRS 1.

2. *CHANDRA* OBSERVATIONS AND DATA REDUCTION

The *Chandra* observation (ObsID 3738) began on 2003 August 12 at 20:59:02 UT and ended on August 13 at 23:29:25 UT, yielding 90,967 s of usable exposure. Pointing was centered near σ Ori AB (HD 37468) at nominal pointing coordinates (J2000.0) R.A. $= 05^{\rm h}38^{\rm m}44.43^{\rm s}$, decl. $= -02^\circ 35' 25.9''$. Grating spectra of σ Ori AB were obtained with the HETG using the ACIS-S detector in faint timed event mode with 3.2 s frame times.

The Level 1 events file provided by the *Chandra* X-Ray Center (CXC) was processed using CIAO version 3.0[1] using standard science threads. The CIAO processing applied calibration updates (CALDB ver. 2.26), selected good event patterns, removed streak artifacts from CCD-8, determined zero-order source centroids, defined grating arm masks and extracted grating spectra, and created response matrix files (RMFs) and auxiliary response files (ARFs) for the extracted spectra. The spectral extraction provides separate dispersed spectra for the medium-energy grating (MEG) and high-energy grating (HEG). The HEG provides higher spectral resolution ($\Delta\lambda = 12$ mÅ FWHM, 1.2–15 Å) than the MEG ($\Delta\lambda = 23$ mÅ, 2.5–31 Å), but the MEG gives a higher signal-to-noise ratio (S/N) in first-order spectra for σ Ori AB. We focus here on the higher S/N data obtained in MEG first-order spectra, combining the +1 and −1 orders for spectral analysis.

In addition, we used the CIAO `wavdetect` tool to identify X-ray sources on the ACIS-S3 chip (CCD-7), which covers a $\approx 8.3' \times 8.3'$ region near the primary target σ Ori AB. We ran `wavdetect` on full-resolution (0.49″ pixels) images using events in the 0.5–7 keV range to reduce the background. The `wavdetect` threshold was set at sigthresh $= 1.5 \times 10^{-5}$, and scale sizes of 1, 2, 4, 8, and 16 were used. We visually compared the `wavdetect` source list against the ACIS-S image and the archived HRC-I image to check for spurious and missed detections.

CIAO `psextract` was used to extract zero-order source and background spectra for brighter sources (>100 net counts). The nominal extraction radius used was $R_e = 4$ pixels (=1.97″). Zero-order light curves were also extracted for brighter sources using CIAO tools. Spectral and timing analyses were undertaken with the HEASOFT Xanadu[2] software package including XSPEC version 12.3.0. We also used a modified version of the ISIS version 1.4.8[3] spectral analysis package to complement the XSPEC analysis. The ISIS implementation allows the flux ratios of the resonance (r), intercombination (i), and forbidden (f) lines in He-like ions to be varied as free parameters when fitting grating spectra. This is an advantage for OB stars since their f/i line flux ratios can be affected by the strong UV radiation field. The modified ISIS package is discussed in more detail by Cohen et al. (2008).

3. X-RAY SOURCE IDENTIFICATION AND PROPERTIES

3.1. *Source Identification*

Our analysis of zero-order data focuses on sources detected on the ACIS-S3 chip (CCD-7), which contains the primary target σ Ori AB. Sources detected on the other chips in the ACIS-S array lie far off-axis and are heavily vignetted and not discussed here. Figure 1 shows the positions of the 42 sources detected on ACIS-S3, and their properties are summarized in Table 2. All of the sources in Table 2 are also visible in the archived HRC-I image (ObsID 2560).

Figure 2 is a zoomed-in view of the ACIS-S3 image in the vicinity of σ Ori AB, the brightest X-ray source on ACIS-S3. The infrared source IRS 1 lying 3.3″ north of σ Ori AB is also detected (CXO 20). Other noteworthy detections are the magnetic B2 Vpe star σ Ori E (CXO 23; § 3.7.2) and the B5 V star HD 37525 (CXO 42), the latter being a known binary (§ 3.7.3). Interestingly, we do not detect the B2 V star σ Ori D even though its spectral type is the same as σ Ori E, a clue that σ Ori E is anomalously bright in X-rays for its spectral type. We do note, however, that an X-ray source at or near the position of σ Ori D is visible in the more sensitive HRC-I image. The A-type star σ Ori C was not detected.

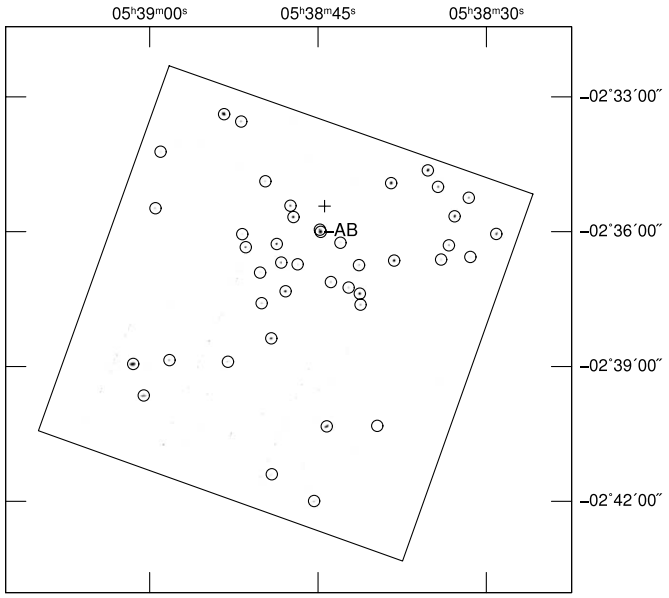

FIG. 1.—Circles mark the positions of the 42 X-ray sources detected on the ACIS-S3 CCD as listed in Table 2. A plus sign marks the *Chandra* aim point, and the primary target σ Ori AB is identified.

All but five of the X-ray sources in Table 2 have optical or near-IR counterparts as determined from a search of the HEASARC object catalogs[4] using a 2″ search radius. As Table 2 shows, the offsets between the X-ray and IR/optical positions are in all cases <1″ and in most cases <0.5″. Interestingly, no IR counterpart was found for CXO 8, which is one of the brighter X-ray sources. However, a faint $V = 20.88$ mag optical source was found in Mayne et al. (2007) at an offset of 0.18″ from the X-ray position. The X-ray source has an unusually hard spectrum (discussed below) and is variable. Further deep optical and infrared observations would be useful to elucidate its nature.

3.2. *Faint Detections and Detection Limit*

The faintest ACIS-S X-ray detection (CXO 32) has 5 ± 2 counts and is confirmed in the HRC-I image. Assuming a slightly more conservative 7 count detection threshold, the corresponding X-ray luminosity threshold determined from PIMMS[5] at a cluster distance $d \approx 390$ pc is $\log L_X = 28.81$ ergs s^{-1} (0.5–7 keV). Here we have assumed a typical late-type pre–main-sequence (PMS) star modeled as an isothermal X-ray source with a Raymond-Smith plasma at $kT = 2$ keV and an absorption column density $N_H = 3 \times 10^{20}$ cm^{-2} [$E(B-V) \approx 0.05$; Gorenstein (1975) conversion].

At a luminosity threshold $\log L_X = 28.81$ ergs s^{-1} we would expect to detect X-ray emission from PMS stars in Orion down to masses of $\sim$0.2–0.3 $M_\odot$, based on previous deep *Chandra* Orion observations (Figs. 3 and 7 of Preibisch et al. 2005). A comparison of the X-ray detections in Table 2 with the optical catalog of Sherry et al. (2004, hereafter S04) confirms this. Two low-mass detections are S04 15 = CXO 17 and S04 18 = CXO 31, both of

[1] Further information on *Chandra* Interactive Analysis of Observations (CIAO) software can be found at http://asc.harvard.edu/ciao.

[2] See http://heasarc.gsfc.nasa.gov/docs/xanadu/xanadu.html.

[3] See http://space.mit.edu/cxc/isis/.

[4] See http://heasarc.gsfc.nasa.gov/docs/archive.html.

[5] For information on PIMMS (Portable Interactive Multi-Mission Simulator) see http://asc.harvard.edu/ciao/ahelp/pimms.html.

TABLE 2
Chandra X-RAY SOURCES IN THE VICINITY OF σ ORI AB

CXO Number	R.A. (J2000.0)	Decl. (J2000.0)	Net Counts	$\langle E \rangle$ (keV)	K_s (mag)	Identification (Offset) (arcsec)
1	05 38 29.12	−02 36 03.0	69 ± 8 (v.99)	1.58	11.69	2M 053829.12−023602.7 (0.30)
2	05 38 31.43	−02 36 33.8	7 ± 3	1.29	10.99	2M 053831.41−023633.8 (0.24)
3	05 38 31.57	−02 35 14.7	32 ± 6	2.07	10.35	2M 053831.58−023514.9 (0.24)
4	05 38 32.83	−02 35 39.4	147 ± 12	1.35	10.73	2M 053832.84−023539.2 (0.30)
5	05 38 33.34	−02 36 18.3	21 ± 5	1.41	11.11	2M 053833.36−023617.6 (0.72)
6	05 38 34.04	−02 36 37.2	8 ± 3	1.10	11.08	2M 053834.06−023637.5 (0.42)
7	05 38 34.31	−02 35 00.2	50 ± 7	1.29	10.35	2M 053834.31−023500.1 (0.12)
8	05 38 35.21	−02 34 38.1	369 ± 19 (v.95)	3.01	...	M07:053835.22−023438.0 (0.18)
9	05 38 38.22	−02 36 38.6	390 ± 20 (v.99)	1.79	10.31	2M 053838.22−023638.4 (0.18)
10	05 38 38.48	−02 34 55.2	697 ± 26 (v.97)	1.60	9.12	2M 053838.49−023455.0 (0.24)
11	05 38 39.72	−02 40 19.2	12 ± 4 (v.96)	3.09	12.88	2M 053839.73−024019.7 (0.54)
12	05 38 41.21	−02 37 37.4	29 ± 5	3.40	14.04	2M 053841.23−023737.7 (0.48)
13	05 38 41.28	−02 37 22.7	323 ± 18	1.64	10.59	2M 053841.29−023722.6 (0.24)
14	05 38 41.35	−02 36 44.6	14 ± 4	1.13	12.08	2M 053841.35−023644.5 (0.12)
15	05 38 42.27	−02 37 14.5	9 ± 3	2.56	10.77	2M 053842.28−023714.7 (0.30)
16	05 38 43.01	−02 36 14.7	6 ± 3	1.93	10.63	2M 053843.02−023614.6 (0.18)
17	05 38 43.85	−02 37 07.3	16 ± 4	1.38	11.77	2M 053843.87−023706.9 (0.54)
18	05 38 44.22	−02 40 20.0	158 ± 13	1.52	10.44	2M 053844.23−024019.7 (0.30)
19	05 38 44.76	−02 36 00.3	2514 ± 50	0.86	4.49	2M 053844.76−023600.2 (0.12); σ Ori AB
20	05 38 44.83	−02 35 57.4	43 ± 7 (v.95)	1.37	...	σ Ori IRS 1
21	05 38 45.35	−02 41 59.6	50 ± 5	1.69	11.04	2M 053845.37−024159.4 (0.42)
22[a]	05 38 46.82	−02 36 43.5	6 ± 2	0.95	12.35	2M 053846.85−023643.5 (0.48)
23	05 38 47.19	−02 35 40.5	454 ± 21 (v.98)	1.56	6.95	2M 053847.20−023540.5 (0.18); σ Ori E
24	05 38 47.46	−02 35 25.4	87 ± 9	1.64	10.72	2M 053847.46−023525.3 (0.18)
25	05 38 47.89	−02 37 19.6	188 ± 14 (v.99)	2.20	10.78	2M 053847.92−023719.2 (0.54)
26	05 38 48.27	−02 36 41.2	42 ± 7	1.35	11.14	2M 053848.29−023641.0 (0.30)
27	05 38 48.68	−02 36 16.4	106 ± 10 (v.95)	1.35	11.17	2M 053848.68−023616.2 (0.18)
28	05 38 49.12	−02 41 23.9	22 ± 6	1.62	...	S04:053849.14−024124.8 (0.96)
29	05 38 49.17	−02 38 22.5	112 ± 11	1.32	10.51	2M 053849.17−023822.2 (0.24)
30	05 38 49.69	−02 34 52.6	8 ± 3	1.22	12.09	2M 053849.70−023452.6 (0.24)
31	05 38 50.02	−02 37 35.5	15 ± 4	1.64	12.10	2M 053850.03−023735.5 (0.18)
32[a,b]	05 38 50.16	−02 36 54.6	5 ± 2	4.06	...	...
33	05 38 51.43	−02 36 20.7	53 ± 7	1.86	11.55	2M 053851.45−023620.6 (0.36)
34	05 38 51.75	−02 36 03.3	6 ± 3	1.56	12.03	2M 053851.74−023603.3 (0.18)
35	05 38 51.85	−02 33 33.0	17 ± 4	2.94	...	...
36	05 38 53.03	−02 38 53.7	12 ± 4	1.50	10.83	2M 053853.07−023853.6 (0.61)
37	05 38 53.37	−02 33 23.2	863 ± 29 (v.99)	1.67	9.73	2M 053853.37−023323.0 (0.24)
38	05 38 58.24	−02 38 51.5	25 ± 5	2.67	...	...
39	05 38 59.03	−02 34 13.2	13 ± 4	2.73	...	...
40	05 38 59.51	−02 35 28.6	12 ± 4	3.06	...	...
41	05 39 00.53	−02 39 38.7	94 ± 10	1.66	11.11	2M 053900.53−023939.0 (0.30)
42	05 39 01.47	−02 38 56.5	342 ± 19	1.42	8.09	2M 053901.50−023856.4 (0.36); HD 37525[c]

NOTES.—Units of right ascension are hours, minutes, and seconds, and units of declination are degrees, arcminutes, and arcseconds. X-ray data are from CCD-7 (ACIS chip S3) using events in the 0.5–7 keV range. Tabulated quantities are running source number, X-ray position (R.A., decl.), net counts and net counts error from `wavdetect` (accumulated in a 90,967 s exposure, rounded to the nearest integer, background subtracted, and PSF corrected), mean photon energy $\langle E \rangle$, K_s magnitude of near-IR 2MASS counterpart, and 2MASS (2M) or optical (S04; M07 = Mayne et al. 2007) candidate counterpart identification within a 2″ search radius. The offset (arcseconds) between the X-ray and counterpart position is given in parentheses. A (v) following net counts error indicates that the source is likely variable as indicated by a variability probability $P_{\rm var} \geq 0.95$ determined from the K-S statistic. The number following v is the K-S variability probability, i.e., v.99 indicates a variability probability $P_{\rm var} = 0.99$. All sources were confirmed to be present in the archived 98 ks *Chandra* HRC-I image (ObsID 2560).

[a] Low-significance `wavdetect` detection (2. < significance < 3.).

[b] Probable *XMM-Newton* counterpart is source NX 99 in Table B.1 of FPS06. High value of $\langle E \rangle$ suggests possible extragalactic background source.

[c] Double star with a B5 V primary and a companion at separation 0.45″ (Caballero 2005).

which have high cluster membership probability (92%–93%). Their mass estimates from S04 are 0.22 $M_\odot$ (S04 15) and 0.18 $M_\odot$ (S04 18), and their respective $V - R_c$ colors imply equivalent main-sequence spectral types of ∼M4 V–M5 V (Kenyon & Hartmann 1995). Also noteworthy is *Chandra* source CXO 22, which was classified as M5 by FPS06 but was listed in their Table A2 (object name B3.01-67) as undetected by *XMM-Newton*.

Some of the faint sources in Table 2 are likely extragalactic background objects. In particular, the five sources without optical or near-IR identifications are extragalactic candidates since all are faint (≤25 counts), nonvariable, and have above average mean photon energies. If we assume a typical extragalactic source power-law X-ray spectrum with a photon power-law index $\Gamma = 1.4$, $N_{\rm H} = 3 \times 10^{20}$ cm^{-2}, and a 7 count detection threshold, then the hard-band (2–8 keV) number counts from the Chandra Deep Field–North (CDF-N) observations (Cowie et al. 2002) predict ≈15 extragalactic sources in the ACIS-S3 CCD field of view above our detection limit. The expression for hard-band (2–8 keV) number counts obtained from CDF-N data by Brandt et al. (2001) gives a similar result. However, the accuracy of the $\log N - \log S$

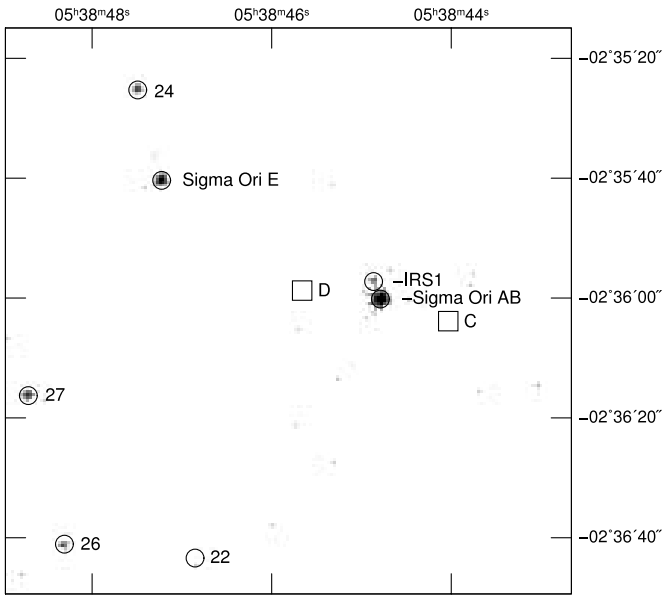

FIG. 2.—Unsmoothed ACIS-S3 image (0.5–7 keV) of the region near σ Ori AB. Circles mark ACIS-S3 detections, and squares mark the optical positions of undetected stars σ Ori C and D. Numbered sources correspond to Table 2.

distribution for extragalactic sources from the Deep Field observations toward lower galactic latitude star-forming regions such as σ Ori ($b \approx -17^\circ$) is not well known. For the deep *Chandra* COUP observation of the ONC ($b \approx -19^\circ$), Getman et al. (2005) concluded that the number of extragalactic sources in the X-ray sample was a factor of $\sim$3–4 less than predicted by CDF number counts.

3.3. *Hardness*

The typical mean photon energy (Table 2) of detected sources is $\langle E \rangle = 1.83$ keV, and the distribution of $\langle E \rangle$ values is shown in Figure 3. The brightest X-ray source σ Ori AB also has the lowest mean energy $\langle E \rangle = 0.86$ keV. The hardest emission is from the very faint source CXO 32 with $\langle E \rangle = 4.06$ keV, for which no optical or IR counterpart was found. These properties suggest that it may be an extragalactic background source.

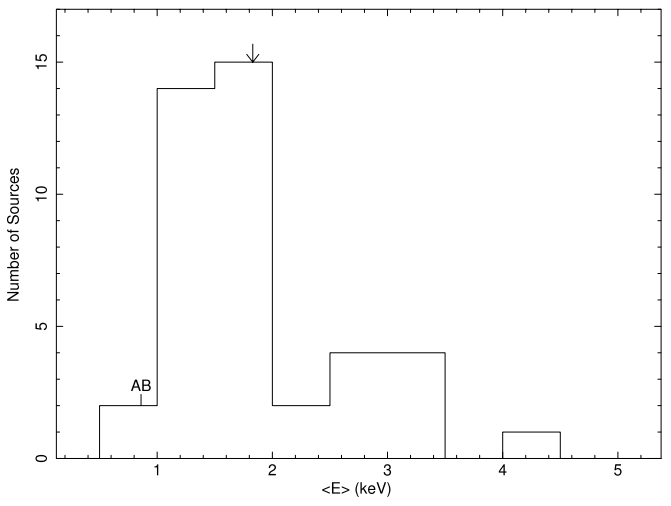

FIG. 3.—Histogram of mean photon energies for X-ray sources on ACIS-S3. The value of σ Ori AB is shown, and the downward-pointing arrow marks the mean value.

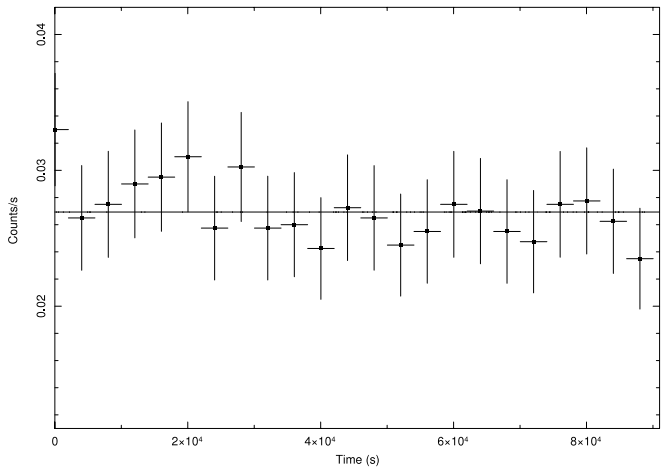

FIG. 4.—ACIS-S3 light curve of σ Ori AB (CXO 19) binned at 4000 s intervals using events in the 0.5–7 keV range and extraction radius $R_e = 1.97''$. The solid line is a best-fit constant count rate model. Error bars are 1 σ. The K-S variability probability is $P_{\rm var} = 0.935$.

3.4. *Variability*

X-ray variability is frequently detected in T Tauri stars. The most extensive data on X-ray variability for young stars in Orion come from the *Chandra* Orion Ultradeep Project (COUP), which obtained a long $\sim$13 day observation of the ONC. Rapid X-ray variability ($\sim$minutes to hours) associated with magnetic reconnection flares was detected in T Tauri stars (Favata et al. 2005), as well as slower X-ray modulation linked to stellar rotation at periods of $\sim$2–12 days (Flaccomio et al. 2005). A variability analysis of 20 massive O, B, and A stars detected in the COUP observation was undertaken by Stelzer et al. (2005). Significant variability was detected in at least six of the nine earliest O7–B3 stars having strong winds. These include known multiple systems that appear to show magnetic behavior such as θ^1 Ori A (B0), θ^2 Ori A (O9.5), and θ^1 Ori C (O7). However, no variability was seen in stars showing the soft X-ray spectra typically associated with radiative wind shocks such as θ^1 Ori D (B0.5) and NU Ori (B1). *Chandra* observations of other massive stars in Orion have also revealed objects with soft X-ray spectra and no detectable variability, such as δ Ori (Miller et al. 2002).

Ten sources detected in our σ Ori observation have high probability of variability as gauged by $P_{\rm var} \geq 0.95$ based on the Kolmogorov-Smirnov (K-S) test (Press et al. 1992) using unbinned photon arrival times. These variable sources are identified in the fourth column of Table 2. The X-ray light curve of σ Ori AB (Fig. 4) shows no evidence of large-amplitude variability. A K-S test on unbinned events gives a variability probability $P_{\rm var} = 0.935$, slightly below the limit $P_{\rm var} \geq 0.95$ that we adopt for variability. A χ^2 test on the light curve binned at 4000 s intervals ($\approx$108 counts bin^{-1}) gives $P_{\rm var} < 0.001$. Thus, we find no evidence for significant ($\geq$95% confidence) X-ray variability in σ Ori AB.

The magnetic B2 Vpe star σ Ori E is variable (Fig. 5; see also § 3.7.2). However, no large flares were detected, in contrast to the large outbursts seen in the *XMM-Newton* observation (Sanz-Forcada et al. 2004) and in the *Chandra* HRC-I exposure. Slow low-amplitude X-ray variability is seen in the unusual hard source CXO 8 (Fig. 6). X-ray flares are clearly visible in CXO 9 (Fig. 7) and CXO 25 (Fig. 8). The counterpart of CXO 9 has been classified as K8 and has properties of a weak-lined T Tauri star (Zapatero Osorio et al. 2002). CXO 25 is associated with an M4 star that has a near-IR excess (Oliveira et al. 2006) indicative of a residual

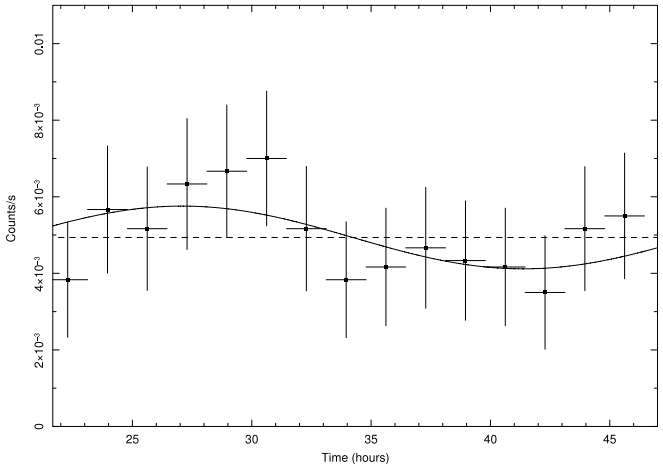

FIG. 5.—ACIS-S3 light curve of σ Ori E (CXO 23) binned at 6000 s intervals using events in the 0.5–7 keV range and extraction radius $R_e = 1.97''$. Error bars are 1 σ. A K-S test gives a high probability of variability $P_{\rm var} = 0.986$. The solid line is a best-fit sinusoid model with a constant offset of 0.004937 counts s^{-1} (*dashed line*) and the period fixed at the stellar rotation period $P_{\rm rot} = 1.19084$ days = 28.58 hr. The time axis shows the elapsed time in hours from start of the day. The *Chandra* observation began at 20:59:02 UT on 2003 August 12 and spanned 1.053 days.

disk or envelope. The second brightest X-ray source in Table 2 (CXO 37) showed a slow decline in count rate by a factor of 2 during the observation, but no large flares.

3.5. *Near-IR Colors*

Figure 9 shows $J - K_s$ colors of those X-ray detections with Two Micron All Sky Survey (2MASS) identifications. IRS 1 was not resolved from σ Ori AB by 2MASS, and no published *JHK* magnitudes are available. Most of the sources lie in the range $0.7 \leq J - K_s \leq 1.3$, typical of early K to late M dwarfs or giants (Bessell & Brett 1988). The three massive stars σ Ori AB, σ Ori E, and the B5 V star HD 37525 are clearly separated in color-magnitude space by their smaller $J - K_s$ and K_s values. An interesting outlier is the faint hard variable X-ray source CXO 12, which has a large value $J - K_s = 2.33$ and is the faintest near-IR identification with $K_s = 14.04$. It is associated with a faint $V = 18.8$ mag optical source (Mayne et al. 2007).

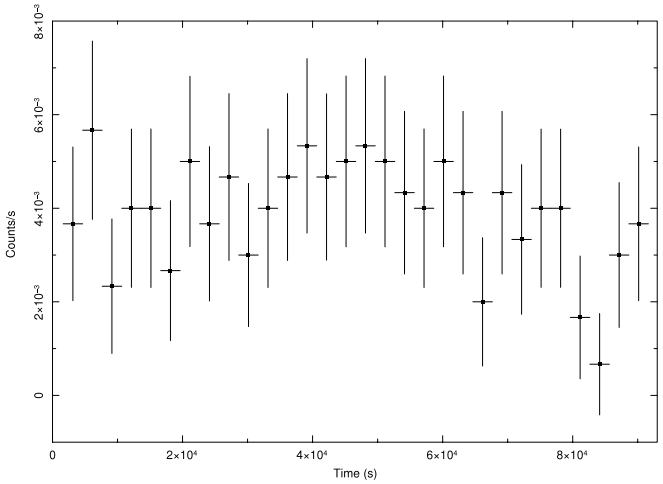

FIG. 6.—ACIS-S3 light curve of the variable source CXO J053835.21−023438.1 (CXO 8) binned at 3000 s intervals using events in the 0.5–7 keV range and extraction radius $R_e = 1.97''$. Error bars are 1 σ. No 2MASS counterpart was found, but a faint $V = 20.88$ mag optical source lies at an offset of $0.18''$ from the X-ray position (Mayne et al. 2007).

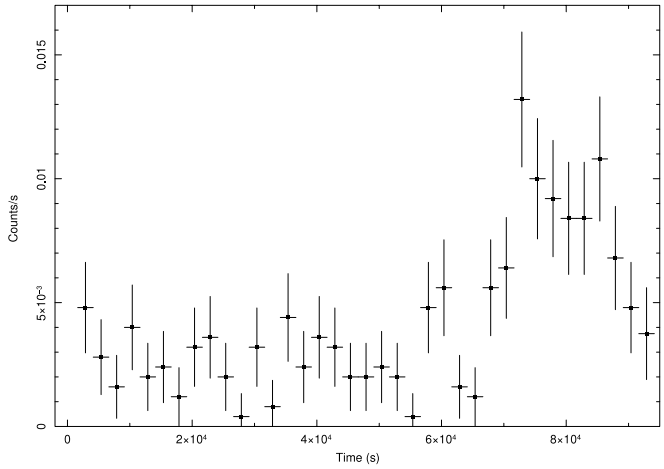

FIG. 7.—ACIS-S3 light curve of CXO J053838.22−023638.6 (CXO 9) binned at 2500 s intervals using events in the 0.5–7 keV range and extraction radius $R_e = 1.97''$. Error bars are 1 σ. This T Tauri star shows weak Hα emission and was classified as K8 by Zapatero Osorio (2002).

Figure 10 is a color-color diagram based on 2MASS JHK_s photometry of X-ray detections with 2MASS identifications. Excluding the three known high-mass stars, 19 of the X-ray sources in Figure 10 have assigned spectral types (FPS06), and all of these are K or M stars. This substantiates the above conclusion that most of the low-mass X-ray detections are K or M stars. Of the 19 X-ray sources with known spectral types, slightly more than half lie to the right of their respective reddening lines as determined from the intrinsic colors of Bessell & Brett (1988) and the extinction law of Rieke & Lebofsky (1985). Thus, in this limited sample of 19 stars, roughly half show evidence of near-IR excesses based on existing spectral type assignments and 2MASS colors.

3.6. *CCD Spectra*

We have fitted the zero-order CCD spectra of brighter sources ($\geq$100 counts) with one-temperature (1T) or two-temperature (2T) APEC solar-abundance optically thin plasma models (Smith et al. 2001) in XSPEC, as summarized in Table 3. We have also fitted the spectrum of the high-interest object IRS 1 (CXO 20), but the fit is not well constrained because this source is faint

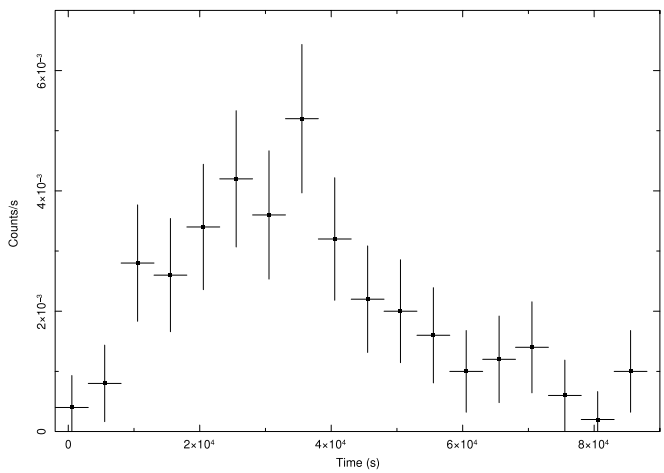

FIG. 8.—ACIS-S3 light curve of CXO J053847.89−023719.6 (CXO 25) binned at 5000 s intervals using events in the 0.5–7 keV range and extraction radius $R_e = 1.97''$. Error bars are 1 σ. This star has been classified as M4 and shows a near-IR excess (Oliveira et al. 2006).

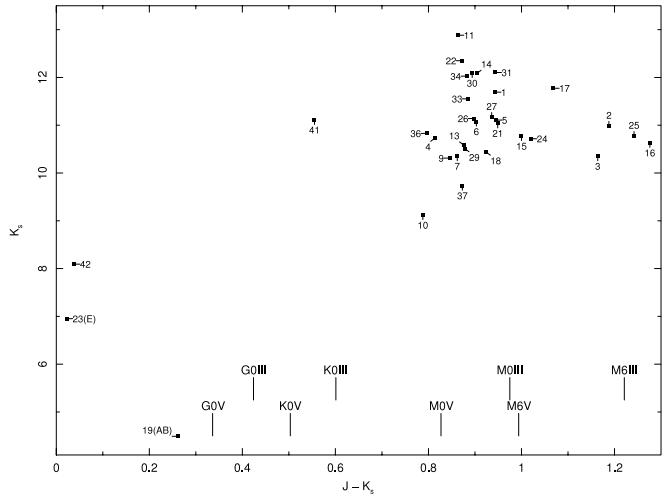

FIG. 9.—Color-magnitude diagram of X-ray sources on ACIS-S3 having 2MASS identifications. Colors are based on 2MASS photometry. Source numbers correspond to Table 2. Intrinsic colors are shown for late-type dwarfs and giants from Bessell & Brett (1988). Source CXO 42 is the B5 V binary star HD 37525. Source CXO 12 is not shown and lies off the right edge of the plot at $(J - K_s, K_s) = (2.33, 14.04)$.

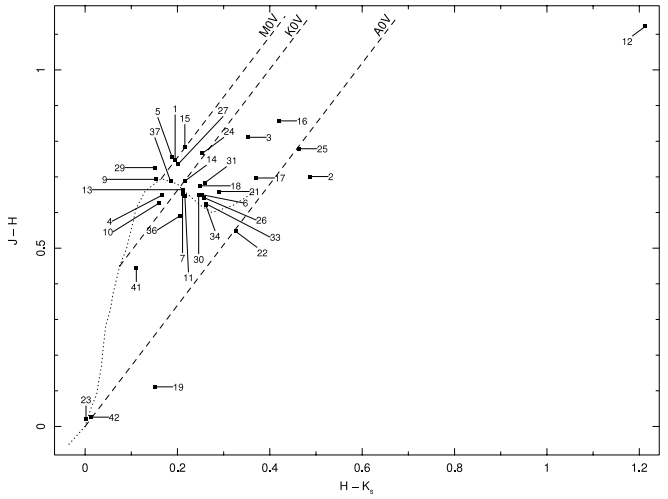

FIG. 10.—Color-color diagram of X-ray sources on ACIS-S3 having 2MASS identifications. Colors are based on 2MASS photometry. Source numbers correspond to Table 2. The dotted line at left marks the unreddened main sequence. The three sloping dashed lines show the loci of M0 V, K0 V, and A0 V stars based on intrinsic colors from Bessell & Brett (1988) and the extinction law of Rieke & Lebofsky (1985).

(43 counts). Photon pileup is low (≈5%) in the zero-order spectrum of σ Ori AB (negligible in first order), and zero-order pileup is negligible (<1.7%) in all the other sources.

In all but a few sources there were insufficient counts to constrain both the temperature and absorption column density, so we held the absorption fixed at $N_{\rm H} = 3 \times 10^{20}$ cm^{-2}, consistent with $E(B - V) \approx 0.05$ mag for the σ Ori region. The best-fit value of $N_{\rm H}$ was within a factor of ≈2 of the above value for the brighter sources where $N_{\rm H}$ was allowed to vary during the fit.

Two-temperature models provide an acceptable approximation to the spectra in most cases. With the notable exception of σ Ori AB (discussed below), the derived temperatures from 2T models are typical of magnetically active PMS stars in the Orion region (Preibisch & Feigelson 2005), showing both a cool component ($kT_1 < 1$ keV) and hotter plasma that is usually in the range $kT_2 \approx 2$–3 keV.

3.7. *Comments on Specific Stars*

3.7.1. *HD 37468* (σ *Ori AB*)

Fits of the CCD spectrum of σ Ori AB excluded events with energies below 0.5 keV to avoid possible contamination from optical light leaks.[6] A simple 1T APEC optically thin plasma model (1T APEC) was not acceptable. However, a 2T APEC model does give an acceptable fit (Fig. 11) with two cool components at $kT_1 = 0.21$ keV and $kT_2 = 0.47$ keV whose emission measure–weighted average is $kT = 0.3$ keV. A fit with the differential emission measure model C6PMEKL in XSPEC using solar abundances gives good results (χ^2/dof = 43.4/44) and shows a single broad peak in the emission measure between 0.2 and 0.3 keV with significant emission measure over the 0.15–0.45 keV range (Fig. 12). Thus, the 2T model is probably an approximation to this broad cool emission measure distribution. The spectrum of σ Ori AB is clearly dominated by cool plasma, consistent with expectations for radiative wind shocks.

[6] The ACIS CCDs are sensitive at optical frequencies, but most optical light is diffracted away from the CCDs by the optical blocking filter. Also, the optical sensitivity is further reduced when the MEG/HEG gratings are in place. Further details can be found at http://www.astro.psu.edu/xray/docs/cal_report/node188.html.

As noted above, *Chandra* does not spatially resolve the A and B components. Thus, our observation does not exclude the possibility that the X-ray emission is the superposition of soft emission from the O9.5 V primary and the B0.5 V secondary. Soft X-ray emission from some B-type stars in Orion has previously been reported, including the B0.5 star θ^1 Ori D (Stelzer et al. 2005).

3.7.2. *HD 37479* (σ *Ori E*)

The helium-strong star σ Ori E has been extensively studied and is known to exhibit optical, UV, and radio modulations at a period $P = 1.1908$ days (Reiners et al. 2000), which has been interpreted as the stellar rotation period. A strong magnetic field that varies from −2.2 to +2.8 kG at the 1.19 day period was detected by Landstreet & Borra (1978) and discussed further by Borra & Landstreet (1979). A distance of 640 pc was obtained by Hunger et al. (1989), which, if correct, would place it behind the σ Ori cluster.

An X-ray flare detected by *ROSAT* was reported by Groote & Schmitt (2004), who concluded that the flare likely occurred on the magnetic B star and not on a hypothesized late-type companion. A large X-ray flare whose rise and decay spanned at least ≈8 hr was also detected by *XMM-Newton* (Sanz-Forcada et al. 2004). The X-ray flare CCD spectrum recorded by the pn camera showed fluorescent Fe emission at ≈6.4 keV, a signature of cool neutral or near-neutral material near the star that was irradiated by hard X-rays during the flare. Sanz-Forcada et al. (2004) argued that an unseen low-mass companion was likely responsible for the flare. A large flare is also visible in the archived *Chandra* HRC-I data.

The *Chandra* ACIS zero-order light curve (Fig. 5) is clearly variable, but no large-amplitude flares were detected. A K-S test gives a variability probability $P_{\rm var} = 0.986$. Low-level modulation may be present in the ACIS light curve, as shown in Figure 5. However, the *Chandra* observation spanned only 88% of the 1.19 day rotation period, and additional time monitoring over more than one period would be needed to substantiate any periodic X-ray modulation.

The *Chandra* ACIS spectrum of σ Ori E (Fig. 13) is definitely harder than that of σ Ori AB, as anticipated from their respective

TABLE 3
SPECTRAL FITS OF ZERO-ORDER ACIS-S3 CCD SPECTRA

CXO Number	N_H (10^{20} cm^{-2})	kT_1 (keV)	kT_2 (keV)	norm$_1$ (10^{-5})	norm$_2$ (10^{-5})	χ^2/dof (χ^2_{red})	Flux (10^{-13} ergs cm^{-2} s^{-1})
4.....	{3.0}	0.37 [0.23–0.51]	1.4 [1.2–1.7]	1.71 [0.67–2.27]	3.32 [2.38–3.99]	5.6/5 (1.12)	0.70 (0.76)
8.....	5.0 [3.8–8.8]	0.69 [0.47–2.16]	19.8 [8.1–. . .]	3.49 [0.10–13.6]	14.1 [12.4–17.4]	32.3/31 (1.04)[a]	1.97 (3.07)
9.....	1.5 [0.0–4.5]	0.61 [0.35–0.78]	2.5 [2.1–2.9]	2.14 [1.44–2.79]	10.4 [9.00–12.0]	31.2/31 (1.01)	1.87 (1.93)
10.....	2.5 [1.2–5.0]	0.70 [0.61–0.76]	2.4 [2.1–2.8]	5.81 [4.83–7.10]	14.4 [12.0–16.3]	72.8/52 (1.40)	3.19 (3.37)
13.....	{3.0}	0.74 [0.63–0.84]	3.1 [2.3–4.8]	2.58 [1.52–3.37]	7.19 [5.53–8.52]	11.4/11 (1.04)	1.55 (1.65)
18.....	{3.0}	0.37 [0.26–0.59]	2.0 [1.6–2.5]	1.89 [0.54–2.56]	3.73 [2.96–4.78]	13.1/14 (0.94)	0.78 (0.84)
19[b]	{3.0}	0.30 [0.29–0.31]	...	111. [105.–116.]	...	76.5/49 (1.56)	15.4 (17.8)
19[b]	{3.0}	0.21 [0.18–0.24]	0.47 [0.45–0.55]	79.9 [69.0–90.9]	41.4 [25.8–50.3]	45.6/47 (0.97)	16.6 (19.5)
20.....	{3.0}	0.61 [0.27–0.83]	2.2 [1.2–. . .]	0.59 [0.27–0.89]	0.61 [0.10–1.11]	1.2/6 (0.20)	0.21 (0.23)
23[c]	{3.0}	0.72 [0.61–0.80]	2.4 [2.0–3.0]	4.43 [3.46–5.24]	8.46 [6.91–10.4]	28.6/24 (1.19)	2.09 (2.23)
25.....	{3.0}	3.20 [2.59–4.09]	...	6.96 [6.07–7.86]	...	18.1/17 (1.06)	0.96 (1.00)
27.....	{3.0}	0.66 [0.49–0.82]	2.2 [1.5–3.4]	1.24 [0.81–1.62]	1.79 [0.96–2.55]	6.4/7 (0.91)	0.50 (0.54)
29.....	{3.0}	0.67 [0.47–0.82]	1.6 [1.1–3.2]	1.29 [0.67–1.89]	1.71 [0.71–2.52]	7.0/8 (0.88)	0.52 (0.56)
37.....	2.1 [0.9–4.1]	0.75 [0.65–0.83]	2.3 [2.1–2.6]	6.02 [4.42–7.06]	24.9 [22.0–27.8]	26.2/32 (0.82)	4.59 (4.80)
42.....	{3.0}	0.76 [0.68–0.83]	2.6 [2.0–3.5]	4.69 [3.65–5.49]	5.56 [4.15–7.37]	34.4/29 (1.19)	1.76 (1.89)

NOTES.—The CXO number in the first column refers to Table 2. Fits are based on one-temperature (1T) or two-temperature (2T) optically thin plasma APEC solar-abundance models of rebinned spectra in XSPEC (ver. 12.3). Solar abundances are referenced to Anders & Grevesse (1989). The notation $N_H = \{3.0\}$ means that the absorption column density was held fixed at that value during fitting. Brackets enclose 90% confidence intervals, and an ellipsis means that the algorithm used to compute the 90% confidence limit did not converge. The norm is related to the volume emission measure (EM) by EM $= 10^{14} 4\pi d_{cm}^2$(norm), where d_{cm} is the distance (cm) to the source. The total X-ray fluxes are the absorbed values in the 0.5–7 keV range, followed in parentheses by unabsorbed values.

[a] An absorbed power-law model with a photon power-law index $\alpha = +1.6$ [1.4–1.8] and $N_H = 2.5 \times 10^{20}$ cm^{-2} gives nearly identical fit statistics with χ^2/dof = 34.7/33 and an unabsorbed flux 2.47×10^{-13} ergs cm^{-2} s^{-1}.

[b] Estimated zero-order photon pileup is 5% for σ Ori AB. Events with energies below 0.5 keV were excluded from the fit to avoid any possible contamination by soft UV/optical leaks.

[c] A 3T APEC model gives an improved fit with $N_H = 2.6$ [1.1–10.4] $\times 10^{20}$ cm^{-2}, $kT_1 = 0.24$ [0.09–0.39] keV, $kT_2 = 0.81$ [0.75–1.05] keV, $kT_3 = 2.6$ [2.1–3.3] keV, norm$_1 = 2.91$ [1.00–12.6] $\times 10^{-5}$, norm$_2 = 3.77$ [2.05–5.42] $\times 10^{-5}$, norm$_3 = 8.11$ [6.73–9.76] $\times 10^{-5}$, χ^2/dof = 18.6/21 ($\chi^2_{red} = 0.89$), and flux = 2.24 (2.41) $\times 10^{-13}$ ergs cm^{-2} s^{-1}.

mean photon energies (Table 2). However, the ACIS spectrum is not as hard as seen by *XMM-Newton* during the flare state, and we do not detect the fluorescent Fe line at 6.4 keV. A 2T APEC model of the ACIS spectrum gives a marginally acceptable fit with a high-temperature component at $kT_2 = 2.4$ keV, which is typical of magnetically active stars. The fit can be improved by using a 3T model and allowing N_H to vary (note to Table 3), and this fit is overlaid in Figure 13. The 3T model gives a temperature $kT_3 = 2.6$ [2.1–3.3; 90% confidence] keV for the hot component, and the inferred value of N_H is consistent with $E(B - V) = 0.05$ (or possibly larger) estimated for this star by Hunger et al. (1989).

The stellar luminosity from the blackbody relation is $L_* = 2.48 \times 10^{37}$ ergs s^{-1}, or $\log(L_*/L_\odot) = 3.81$, where we have assumed $T_{eff} = 22{,}500$ K and $R_* = 5.3^{+1.35}_{-1.1}\ R_\odot$ from Hunger et al. (1989). The unabsorbed flux from the 3T model gives an X-ray luminosity $L_X(0.5\text{–}7\ \text{keV}) = 2.88 \times 10^{25} d_{pc}^2$, where d_{pc} is the distance in parsecs. Adopting $d = 640$ pc (Hunger et al. 1989) gives $\log(L_X/L_*) = -6.32$. This ratio is much higher than usually found for B2 V stars, for which a catalog of *ROSAT* detections gives typical values $\log(L_X/L_*) \approx -7.2$ to -6.8 (Berghöfer et al. 1996). In fact, these typical values are too large since the *ROSAT* All Sky Survey (RASS) was based on short exposures and thus

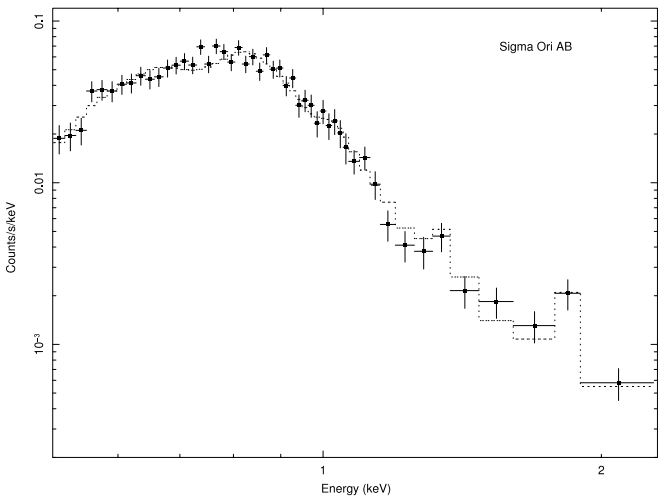

FIG. 11.—Zero-order CCD spectrum of σ Ori AB rebinned to a minimum of 20 counts bin^{-1}. The dotted line shows the best-fit 2T APEC model with fit parameters as listed in Table 3.

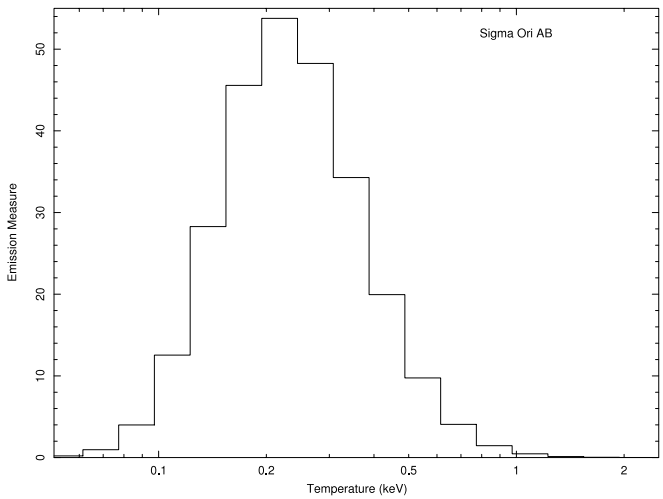

FIG. 12.—Emission measure distribution of σ Ori AB obtained from a best fit of the zero-order CCD spectrum with the XSPEC model C6PMEKL using solar abundances and hydrogen column density $N_H = 3 \times 10^{20}$ cm^{-2}.

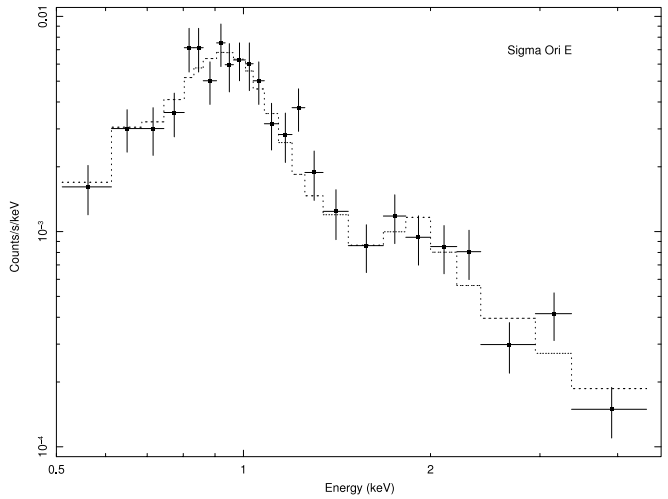

FIG. 13.—Zero-order CCD spectrum of σ Ori E rebinned to a minimum of 15 counts bin^{-1}. The dotted line shows the best-fit 3T APEC model with fit parameters as listed in Table 3 notes.

selected in favor of the detection of X-ray–bright B2 V stars. A ratio $\log(L_X/L_*) \approx -8$ may actually be more representative (Cohen et al. 1997). This strengthens the conclusion that the value of L_X/L_* for σ Ori E at $d = 640$ pc is anomalously large for a B2 V star. This is a clue that the star may actually lie in the σ Ori cluster instead of behind it.

If σ Ori E lies in the cluster at $d \sim 390$ pc, then $\log(L_X/L_*) = -6.75$. This is in better agreement with other B2 V stars, but still at the high end of the range. Taking into account the uncertainty in the X-ray flux measurement from the 3T APEC fit ($\approx$15%), the uncertainty in R_* (see above), and allowing for a slightly higher temperature $T_{\rm eff} = 23{,}500$ adopted in some studies (Nakajima 1985; Groote & Schmitt 2004), the above ratio could be as low as $\log(L_X/L_*) = -7.09$. Thus, uncertainties could conspire to decrease the L_X/L_* ratio to a value that is within the range found for X-ray–bright *ROSAT* B2 V star detections.

In summary, the L_X/L_* ratio for σ Ori E is anomalously high compared to other B2 V stars if it lies at $d = 640$ pc. If the star lies in the cluster at $d = 390$ pc, the ratio is in better agreement with that of other X-ray–luminous B2 V stars, but still at the high end of the range if the nominal stellar parameters are adopted. These indications that the L_X/L_* ratio is high and persistent X-ray flaring leave open the possibility that a late-type companion may be contributing to the X-ray emission of σ Ori E. High angular resolution searches for a close companion are warranted.

The rather high plasma temperature for this star and its X-ray variability are not consistent with radiative wind shock predictions. The detection of a strong magnetic field gives reason to believe that the magnetically confined wind shock (MCWS) picture may be relevant. This model is capable of producing higher plasma temperatures than the conventional radiative wind shock scenario and was originally formulated to explain hot plasma in stars with strong $\sim$kG magnetic fields such as the Ap star IQ Aur (Babel & Montmerle 1997a, hereafter BM97a). It has also been invoked to explain hard rotationally modulated X-ray emission in the young magnetic O star θ^1 Ori C (Babel & Montmerle 1997b; Donati et al. 2002; Gagné et al. 2005; Schulz et al. 2000). The good agreement between model predictions and observed X-ray parameters for θ^1 Ori C found by Gagné et al. (2005) provides solid support for the MCWS interpretation.

In the MCWS picture, a strong surface magnetic field can channel the wind flow into two oppositely directed streams from each hemisphere, which collide near the magnetic equator and liberate their kinetic energy in shock-heated plasma. The degree to which the wind is confined by the magnetic field is expressed in terms of the confinement parameter $\eta = B_{\rm eq}^2 R_*^2/\dot{M}v_\infty$, where $B_{\rm eq}$ is the equatorial magnetic field strength (ud-Doula & Owocki 2002). For $B \sim 2$ kG and plausible mass-loss parameters (Groote & Hunger 1997), one obtains $\eta \gg 1$ for σ Ori E. That is, the wind is strongly confined by the magnetic field.

Building on earlier work, Townsend et al. (2005) extended the MCWS idea into a rigidly rotating magnetosphere model. They showed that by allowing the center of a dipole magnetic field to be displaced away from the center of the star, many aspects of the periodic behavior of σ Ori E could be explained. This work has now been expanded into a rigid field hydrodynamics (RFHD) approach by Townsend et al. (2007). The RFHD approach is relevant to stars with strong magnetic fields such as σ Ori E where the wind has little effect on the field lines.

Numerical RFHD simulations of the X-ray emission of a generic star with properties similar to σ Ori E by Townsend et al. (2007) predict hot plasma with an emission measure distribution peaking near $kT \approx 3.5$ keV. This is somewhat hotter than we infer from our best-fit 3T model, which gives $kT_3 = 2.6$ [2.1–3.3; 90% conf.] keV. However, as Townsend et al. (2007) have noted, the higher temperature in the RFHD model could be a consequence of uncertainties in the mass-loss parameters and neglecting thermal conduction effects. Future refinements of the RFHD model tailored specifically to σ Ori E will address these temperature differences and also have the potential to provide theoretical estimates of the X-ray luminosity and X-ray absorption that can be directly compared with observations.

3.7.3. *HD 37525*

This star is classified as B5 V and has a known companion at a separation of $0.45'' \pm 0.04''$ (Caballero 2005). The *Chandra* ACIS-S spatial resolution is not sufficient to distinguish between the primary and the companion. However, if the companion is a PMS star (Caballero 2005), then it likely contributes to the X-ray emission.

3.7.4. *σ Ori IRS 1*

IRS 1 lies $3.3''$ north-northeast of σ Ori AB and was discovered in subarcsecond mid-IR observations with the ESO 3.6 m telescope by van Loon & Oliveira (2003). It shows a clear near- to mid-IR excess indicative of a disk. The mid-IR emission was resolved into an elongated structure extending away from σ Ori AB that was described as "fan shaped" by van Loon & Oliveira (2003). The unusual elongated structure and small angular separation between IRS 1 and σ Ori AB support the conclusion that the two objects are physically associated and that circumstellar material around IRS 1 is being influenced by the strong OB system radiation field.

Observational evidence for the source now known as IRS 1 was in fact already present in earlier VLA radio observations obtained by Drake (1990). No radio source was detected at the optical position of σ Ori AB, but he reported a radio source at J2000.0 position R.A. $= 5^{\rm h}38^{\rm m}44.78^{\rm s}$, decl. $= -2^\circ 35' 57.6''$. This source lies $\approx 2.7''$ north-northeast of σ Ori AB but is offset by only $\approx 1''$ from the IRS 1 8.6 μm peak (Fig. 1 of van Loon & Oliveira 2003). Thus, an association between the radio source and IRS 1 seems likely.

The 6 cm flux densities reported by Drake (1990) are much larger than would be expected for free-free wind emission from σ Ori AB, and this provides additional support that the radio source is not σ Ori AB. Adopting the wind parameters for σ Ori AB

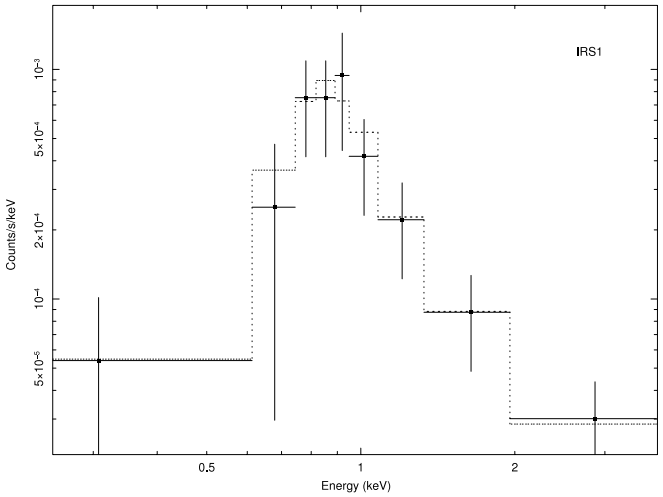

FIG. 14.—ACIS-S3 CCD spectrum of σ Ori IRS 1 (CXO 20) binned to 5 counts bin^{-1}. The dotted line shows the 2T APEC model with fit parameters as listed in Table 3.

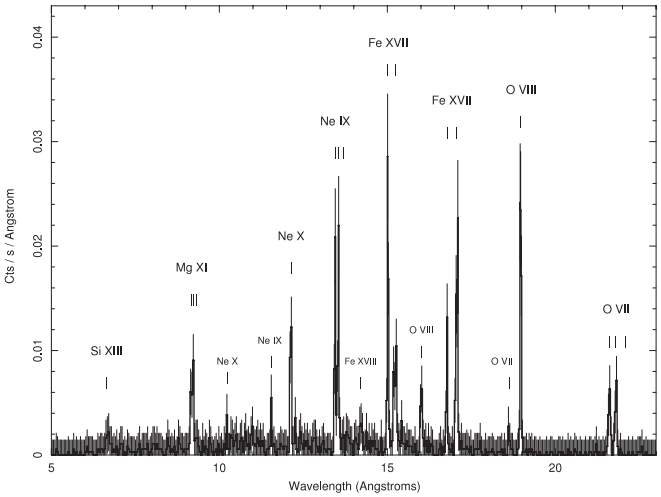

FIG. 15.—HETG/MEG1 background-subtracted spectrum (+1 and −1 orders combined; 1936 net counts) of σ Ori AB with prominent lines identified.

in Table 1, the predicted 6 cm radio flux density for free-free emission from a spherical fully ionized wind is $S_{4.86\ \mathrm{GHz}} = 0.1$ mJy (eq. [7] of Skinner et al. 1993). This value is a factor of 15–20 smaller than the observed flux density of the detected radio source (Table 2 of Drake 1990). The upper limit on the radio flux density measured at the position of σ Ori AB in VLA images is $S_{4.86\ \mathrm{GHz}} \leq 0.3$ mJy (S. Drake 2008, private communication), which is consistent with the predicted 0.1 mJy flux density for free-free wind emission.

Chandra's high angular resolution clearly reveals a faint X-ray source (CXO 20) located 2.85″ north and 0.93″ east of σ Ori AB, which we associate with IRS 1 (Fig. 2). Only 43 net counts were detected from this X-ray source, but this provides enough information to undertake a rudimentary spectral analysis. The CCD spectrum (Fig. 14) is absorbed below ≈0.7 keV and peaks at $E \approx 1$ keV. Spectral fits imply hotter plasma at $kT > 1$ keV (Table 3). The unabsorbed X-ray luminosity of IRS 1 is $L_{\mathrm{X}}(0.5\text{–}7\ \mathrm{keV}) = 2.75 \times 10^{24} d_{\mathrm{pc}}^2$ (ergs s^{-1}), where d_{pc} is the distance in parsecs. Assuming that IRS 1 is physically associated with σ Ori AB at a distance of ∼352 pc, one obtains $\log L_{\mathrm{X}}(0.5\text{–}7\ \mathrm{keV}) = 29.53$ ergs s^{-1}. The K-S test gives a high variability probability $P_{\mathrm{var}} = 0.95$ for IRS 1. A coarse light curve binned at 11,000 s intervals (9 bins with ≈5 counts bin^{-1}) shows a slow increase in count rate by a factor of ∼3 during the last 70 ks of the observation, but with large count rate uncertainties because of the faint emission. The likely presence of variable X-ray emission from IRS 1 at a plasma temperature of $kT \approx 1$ keV (and perhaps higher) demonstrates that the infrared source detected by van Loon & Oliveira (2003) harbors a magnetically active young star.

The *Chandra* COUP study has shown that the X-ray luminosity of optically revealed PMS stars in the Orion Nebula correlates with mass, albeit with large scatter (Preibisch et al. 2005). Assuming a similar correlation for the σ Ori cluster, the above L_{X} along with the mid-IR data would imply that IRS 1 is likely a T Tauri star with a mass of a few tenths of a solar mass whose disk/envelope is being photoevaporated in the harsh UV environment of σ Ori AB.

3.7.5. *Source CXO 8* (*J053835.21−023438.1*)

A thermal plasma model requires a very high temperature for the variable source CXO 8, but a simple absorbed power-law model also gives an acceptable fit (Table 3). We find no counterpart in HEASARC extragalactic catalogs, but the X-ray source lies at a small offset from a faint $V = 20.88$ mag optical source (Mayne et al. 2007).

4. GRATING SPECTRUM OF σ Ori AB

4.1. *General Properties*

Figure 15 shows the first-order MEG1 spectrum of σ Ori AB with prominent lines identified. Line properties are summarized in Table 4.

In order to test the feasibility of various emission models (§ 5), we need information on X-ray temperature, line widths, line centroid shifts (if any), and flux ratios of specific lines. Information on line shape is also important, since radiative wind shock models predict line asymmetries for optically thick winds. But at the S/N of the MEG1 spectrum, the lines can be acceptably fitted with Gaussians and we do not find any conclusive evidence of line asymmetries.

The spectrum is clearly dominated by lines from relatively cool plasma, with the coolest lines being the O VII He-like triplet *r* and *i* lines and the O VII line at 18.627 Å ($\log T_{\mathrm{max}} = 6.3$ K). The highest temperature and shortest wavelength line detected was Si XIII ($\lambda_{\mathrm{lab}} = 6.6479$ Å; $\log T_{\mathrm{max}} = 7.0$ K).

4.2. *Line Widths*

Line fluxes and widths were based on fits with a weak power-law component plus a Gaussian profile convolved with the instrumental response. The weak power-law component accounts for faint emission outside the line, due to either true continuum or a pseudocontinuum arising from many faint unresolved lines.

The strongest lines based on observed line flux are O VIII ($\lambda_{\mathrm{lab}} = 18.967$ Å) and the O VII intercombination line ($\lambda_{\mathrm{lab}} = 21.804$ Å). In general, all lines for which widths could be reliably measured are moderately broadened in excess of thermal (Doppler) widths, the latter being no greater than ∼60 km s^{-1} for the detected ions at a temperature $T \sim 3.5$ MK.

Gaussian fits of nine prominent lines give a mean half-width at half-maximum $\overline{\mathrm{HWHM}} = 264 \pm 80$ (1 σ) km s^{-1}. Spectral fits with ISIS give nearly identical results. Taking the uncertainties of the line width measurements into account, there is no clear dependence of line width on wavelength or maximum line power temperatures T_{max} (Figs. 16 and 17).

The mean HWHM for σ Ori AB is much less than observed for O supergiants (Fig. 6 of Cohen et al. 2003), slightly less than for

TABLE 4
σ Ori AB Emission Line Properties

Ion	λ_{lab} (Å)	λ_{obs} (Å)	$\Delta\lambda$ (mÅ)	Line Flux (10^{-5} photons cm^{-2} s^{-1})	HWHM (km s^{-1})	log T_{max} (K)
Si XIII (*r*).....	6.6479	...	...	0.12 (0.01–0.22)	{300}	7.0
Mg XI (*r*)	9.1687	9.165 (9.162–9.169)	−4.	0.42 (0.30–0.55)	250 (8–374)	6.8
Mg XI (*i*).....	9.2312	...	...	0.41 (0.27–0.52)	250[a]	6.8
Mg XI (*f*).....	9.3143	...	...	...[b]	...	6.8
Ne X.....	10.239	...	...	0.25 (0.09–0.42)	{300}	6.8
Ne IX.....	11.544	...	...	0.48 (0.23–0.74)	{300}	6.6
Ne X[c]	12.132	12.127 (12.124–12.130)	−5.	1.64 (1.28–1.98)	390 (248–542)	6.8
Ne IX (*r*)	13.447	13.446 (13.441–13.449)	−1.	3.36 (2.80–4.03)	314 (216–381)	6.6
Ne IX (*i*)	13.553	13.546 (13.543–13.548)	−7.	3.53 (2.87–4.09)	314[a]	6.6
Ne IX (*f*).....	13.699	...	...	...[b]	...	6.6
Fe XVII	15.014	15.013 (15.010–15.016)	−1.	7.94 (6.69–9.14)	279 (195–355)	6.7
O VIII.....	15.176	...	...	1.11 (0.53–1.98)	{300}	6.5
Fe XIX	15.198	...	...	1.01 (0.55–2.24)	{300}	6.9
Fe XVII	15.261	15.258 (15.251–15.266)	−3.	3.09 (2.36–3.83)	{300}	6.7
O VIII.....	16.006	16.009 (16.002–16.015)	+3.	2.63 (1.57–3.60)	195 (0–405)	6.5
Fe XVII	16.780	16.778 (16.772–16.785)	−2.	4.98 (3.66–6.27)	155 (21–278)	6.7
Fe XVII	17.051	17.049 (17.043–17.055)	−2.	5.32 (4.15–6.63)	163 (92–240)	6.7
Fe XVII	17.096	17.091 (17.086–17.096)	−5.	6.91 (5.58–8.29)	{163}	6.7
O VII	18.627	...	...	1.86 (0.25–3.46)	{300}	6.3
O VIII[c]	18.967	18.968 (18.964–18.972)	+1.	22.0 (19.6–27.8)	330 (273–435)	6.5
O VII (*r*).....	21.602	21.608 (21.598–21.617)	+6.	15.5 (10.7–21.8)	298 (97–507)	6.3
O VII (*i*).....	21.804	21.803 (21.796–21.810)	−1.	22.4 (15.2–30.1)	298[a]	6.3
O VII (*f*)	22.098	...	...	...[b]	...	6.3

Notes.—X-ray data are from the background-subtracted HETG/MEG1 spectrum (+1 and −1 orders combined), regrouped to a minimum of 10 counts bin^{-1}. Parentheses enclose 1 σ intervals. Tabulated quantities are ion name (Ion), where *r*, *i*, *f* denote resonance, intercombination, and forbidden lines, respectively; laboratory wavelength of transition (λ_{lab}); measured wavelength (λ_{obs}); $\lambda_{obs} - \lambda_{lab}$ ($\Delta\lambda$); observed (absorbed) continuum-subtracted line flux (Line Flux); line half-width at half-maximum (HWHM); and maximum line power temperature (T_{max}). An ellipsis means that λ_{obs} was not measured due to faint or closely spaced lines. Braces enclose quantities that were held fixed during fitting. The value of λ_{obs} is subject to the ±11 mÅ absolute wavelength calibration accuracy of MEG.

[a] The line width was allowed to vary during fitting but was kept equal to the width of the resonance (*r*) line.

[b] The forbidden line was undetected.

[c] Blend.

the O9.5 II star δ Ori (HWHM = 430 km s^{-1}; Miller et al. 2002), very similar to that of the B0.2 V star τ Sco (Cohen et al. 2003), but slightly larger than found for the B0.5 III star β Cru (HWHM $\approx$ 150 km s^{-1}; Cohen et al. 2008). Although there is considerable scatter in the line widths for any particular star and

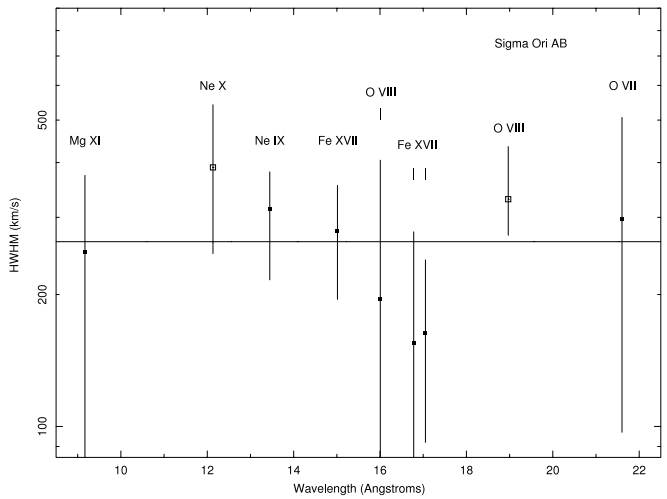

Fig. 16.—Measured line widths of σ Ori AB expressed as half-width at half-maximum (1 σ error bars) vs. line laboratory wavelength using data from Table 4. The two lines shown with open squares are blends, and their HWHM values are likely overestimated. The solid horizontal line is the mean value $\overline{\text{HWHM}} = 264$ km s^{-1}.

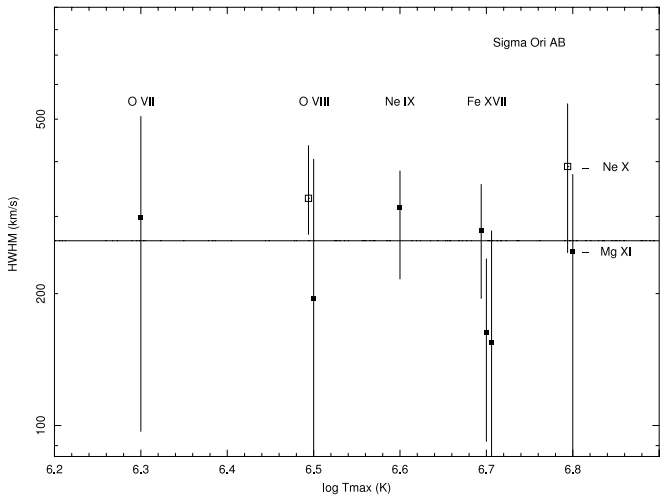

Fig. 17.—Measured line widths of σ Ori AB expressed as half-width at half-maximum (1 σ error bars) vs. maximum line power temperature T_{max} using data from Table 4. The plotted values of T_{max} for O VIII, Fe XVII, and Ne X have been shifted slightly from the nominal values given in Table 4 to avoid error bar overlap. The two lines shown with open squares are blends, and their HWHM values are likely overestimated. The solid horizontal line is the mean value $\overline{\text{HWHM}} = 264$ km s^{-1}.

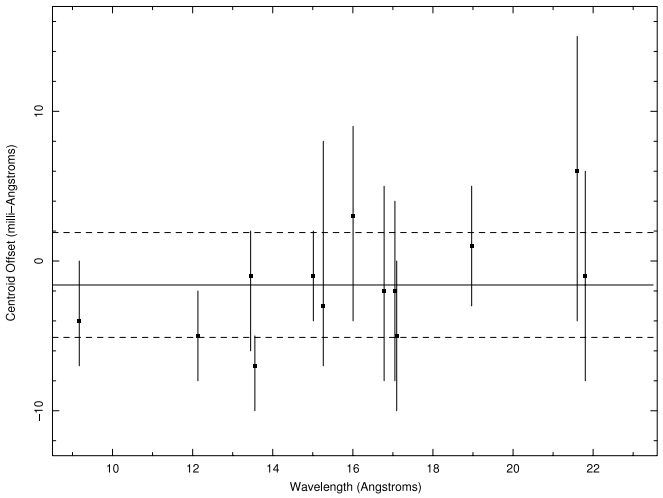

FIG. 18.—Plot of the centroid offset between the measured and laboratory line centroid of prominent lines in the MEG1 spectrum, using the offset values $\Delta\lambda = \lambda_{obs} - \lambda_{lab}$ from Table 4. Errors bars are 1 σ. The mean offset (*solid line*) and ± 1 σ uncertainty (*dashed lines*) for 13 measurements are -1.6 (± 3.5) mÅ.

the sample is still small, these results suggest tentatively that there is a trend for broader lines in O stars with stronger winds versus B stars with weaker winds. The mean HWHM value for σ Ori AB is well below the terminal wind speed $v_\infty \approx 1060$ km s^{-1} (Howarth & Prinja 1989). Expressed as a ratio, the value from individual line fits gives $\overline{\mathrm{HWHM}}/v_\infty = 0.22$–$0.25$. These ratios are comparable to the value 0.22 found for δ Ori (Miller et al. 2002).

4.3. *Line Centroids*

Gaussian line centroids were measured for 13 stronger lines. In all cases the centroids lie within 7 mÅ of the laboratory values and for eight lines the offsets are ≤ 3 mÅ, as shown in Figure 18. These offsets are well within the ± 11 mÅ absolute wavelength calibration accuracy of MEG1.[7] Both positive and negative offsets were found with 10 lines blueshifted and three redshifted. The mean centroid offset was -1.6 ± 3.5 (± 1 σ) mÅ. In only

[7] *Chandra* Proposer's Observatory Guide: http://asc.harvard.edu/proposer/POG/.

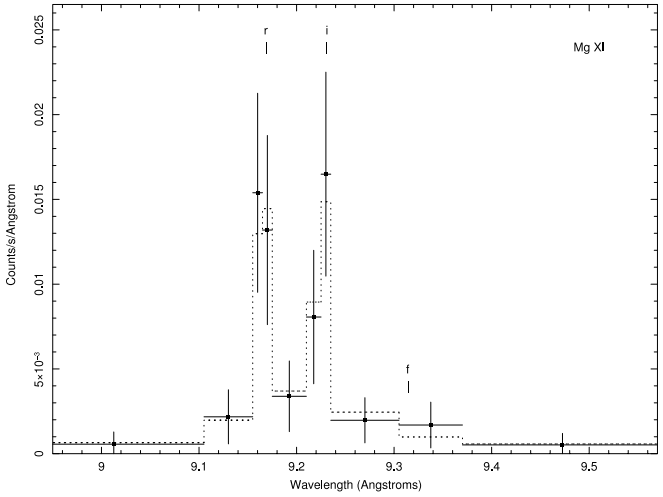

FIG. 19.—Histogram plot of the MEG1 spectrum (+1 and -1 orders combined) of σ Ori AB near the Mg XI He-like triplet, binned to a minimum of 10 counts bin^{-1}. Filled squares are data points, and the dotted line is a Gaussian fit with weak power-law continuum. The resonance (*r*) and intercombination (*i*) lines are detected, but the forbidden (*f*) line is not.

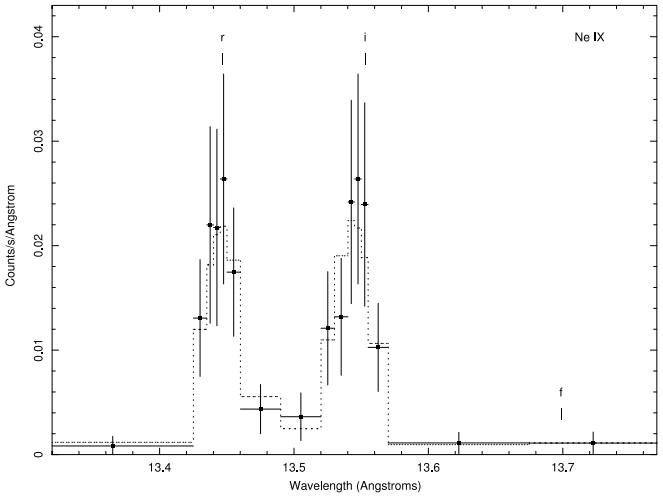

FIG. 20.—Histogram plot of the MEG1 spectrum (+1 and -1 orders combined) of σ Ori AB near the Ne IX He-like triplet, binned to a minimum of 10 counts bin^{-1}. Filled squares are data points, and the dotted line is a Gaussian fit with weak power-law continuum. The resonance (*r*) and intercombination (*i*) lines are detected, but the forbidden (*f*) line is not.

two cases does λ_{lab} lie outside the $\pm 1\sigma$ uncertainty interval of the measured centroid. The centroid measurements of these two lines are uncertain due to close blends (Ne X λ12.1321/λ12.1375) and possible contamination by weak nearby Fe lines (Ne IX λ13.553).

4.4. *Helium-like Ions*

He-like triplets show strong resonance (*r*) and intercombination (*i*) lines, but the forbidden (*f*) lines are very faint and formally undetected. The resonance and intercombination lines were detected in the Mg XI (Fig. 19), Ne IX (Fig. 20), and O VII (Fig. 21) He-like triplets. The Si XIII resonance line was detected, but the emission in the triplet is so faint that no reliable diagnostic information can be obtained apart from an estimate of the resonance line flux. The strong *i* lines and faint or absent *f* lines are a clear indication that the *f* and *i* line fluxes are being affected by the strong UV radiation field of σ Ori A ($T_{\mathrm{eff}} = 33{,}000$ K; Howarth & Prinja 1989).

In general, the line flux ratio $R = f/i$ is sensitive to both electron density *n* and the UV radiation field (Gabriel & Jordan 1969).

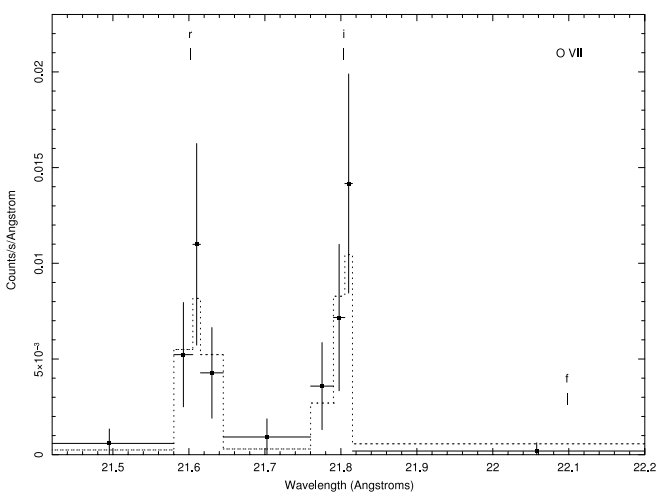

FIG. 21.—Histogram plot of the MEG1 spectrum (+1 and -1 orders combined) of σ Ori AB near the O VII He-like triplet, binned to a minimum of 10 counts bin^{-1}. Filled squares are data points, and the dotted line is a Gaussian fit with weak power-law continuum. The resonance (*r*) and intercombination (*i*) lines are detected, but the forbidden (*f*) line is not.

TABLE 5
σ Ori AB He-like Ion Line Flux Ratios

Parameter	Mg XI	Ne IX
$\lambda_{lab,r}$ (Å).....	9.1687	13.447[a]
log T_{max} (K).....	6.8	6.6
G[b].....	1.21 [0.76–1.92]	0.99 [0.73–1.32]
R[b].....	≤0.17	≤0.15
R_0	2.7	3.6
ϕ_c (s^{-1}).....	4.86×10^4	7.73×10^3
n_c (cm^{-3}).....	6.2×10^{12}	6.4×10^{11}
r_{fi}/R_*	≤1.8	≤4.4

Notes.—The laboratory rest wavelength of the resonance line $\lambda_{lab,r}$ and the maximum line power temperature T_{max} are from APED. The line flux ratios $G = (f + i)/r$ and $R = f/i$ are from ISIS spectral fits (see below). R_0 is the theoretical limit of R at T_{max} for low photoexcitation and low density (Ne IX from Pradhan 1982; Mg XI from Porquet et al. 2001). The critical photoexcitation rate ϕ_c and critical density n_c are from BDT72. The 90% confidence upper limit on the line formation radius is r_{fi}/R_*.

[a] The Ne IX resonance line may be weakly contaminated by emission from Fe XIX (13.462 Å).

[b] Determined from simultaneous fits of MEG1+HEG1 spectra with ISIS. The He-like complexes were fitted allowing R, G, and the metal abundances to vary. ISIS applies the appropriate instrumental and thermal broadening to each line. The best-fit abundances of Mg and Ne are consistent with solar at the 90% confidence level. The continuum level was determined by a global 2T VAPEC fit of the zero-order spectrum. Square brackets enclose 90% confidence intervals on G, and upper limits on R are 90% confidence.

If ϕ is the photoexcitation rate from the $^3S_1$ level to the $^3P_{2,1}$ levels, then $R = R_0/[1 + (\phi/\phi_c) + (n/n_c)]$, where ϕ_c and n_c are the critical photoexcitation rate and critical density. The quantities R_0, ϕ_c, and n_c (Table 5) depend only on atomic parameters and the electron temperature of the source, as defined in Blumenthal et al. (1972, hereafter BDT72).

In hot star winds, densities $n > n_c$ high enough to affect R would only occur very close to the star, and it is thus reasonable to assume that any observed reduction in R relative to R_0 is the result of photoexcitation by the hot star UV radiation field. Thus, in hot stars the value of R is not a reliable density diagnostic but is instead a measure of the photoexcitation rate in the line-emitting region and can be used along with atmospheric models to constrain the distance from the star at which the He-like triplet line is formed. In cool stars with negligible UV flux, the value of R can be used to constrain the density. In the limit of low photoexcitation ($\phi \ll \phi_c$) and low density ($n \ll n_c$), $R \rightarrow R_0$.

For the He-like ions detected in the MEG spectrum of σ Ori AB, the most stringent limit on the line formation radius based on the measured upper limit of R comes from the Mg XI triplet. We have used a solar abundance TLUSTY model atmosphere (Lanz & Hubeny 2007) with $T_{eff} = 32{,}500$ and $\log g = 4.0$, along with the formalism in BDT72 and Leutenegger et al. (2006), taking an average of the photospheric fluxes of the two ^3S–$^3P_{1,2}$ transitions (997.5 and 1034.3 Å for Mg XI). We have averaged these fluxes over ≈3 Å blueward of these wavelengths to account for the Doppler shift in the wind (Leutenegger et al. 2006). We find an expression for the ratio $R(r) = f/i$ as a function of the distance r from the center of the star, which takes into account the dilution factor $W(r)$ and is plotted in Figure 22.

For Mg XI our spectral fits give a 90% confidence upper limit $R = f/i \leq 0.17$ (Table 5). As can be seen in Figure 22, this upper limit implies a small line formation radius $r \leq 1.8R_*$, where, as usual, r is measured from the center of the star. A similar analysis for Ne IX gives $R \leq 0.15$ and a formation radius $r \leq 4.4R_*$. The

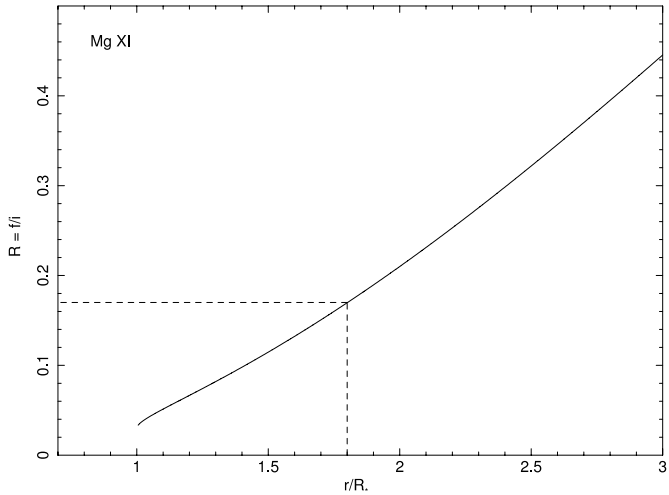

Fig. 22.—Ratio of forbidden to intercombination Mg XI line fluxes for σ Ori AB as a function of distance from the center of the star. The horizontal axis expresses the distance in units of the stellar radius, where $R_* = 9\ R_\odot$. The solid line shows the predicted $R = f/i$ flux ratio based on a TLUSTY atmospheric model with $T_{eff} = 32{,}500$ K (see text). The vertical dashed line marks the 90% upper limit on the line formation radius $r_{fi} < 1.8R_*$ (referenced to the center of the star) based on the limit $R < 0.17$ determined from spectral fits (Table 5).

O VII triplet does not provide a useful constraint on the line formation radius. Using the adopted mass-loss parameters in Table 1 and an estimated wind X-ray opacity $\kappa_w \approx 80\ cm^2\ g^{-1}$ near $E \approx 1$ keV (Waldron et al. 1998; Cohen et al. 1996; Ignace et al. 2000), the wind is expected to be optically thin at $E \approx 1$ keV down to the stellar surface. In addition, our modeling of the Fe XVII line (15.014 Å) confirms that the wind optical depth is consistent with zero. Thus, X-rays formed at the small radii given above could escape through the wind.

4.5. *Abundances*

We have simultaneously fitted the zero-order spectrum and the MEG1 and HEG1 first-order spectra of σ Ori AB to search for significant deviations from solar abundances. These fits were conducted using an absorbed 2T VAPEC model with a modified version of ISIS (Cohen et al. 2008) that allows the R and G ratios of He-like triplets to be fitted as free parameters. We allowed the abundances of elements with prominent lines in the spectrum to vary, namely, O, Ne, Mg, Si, and Fe. We found no significant deviations from solar abundances. The largest deviation found was for magnesium, which gave a best-fit abundance Mg = 0.78 [0.62–1.08; 90% conf.] times solar.

4.6. *Summary of Grating Spectra Results*

In summary, the key properties determined from the spectral analysis of σ Ori AB are (1) dominant cool plasma ($kT \approx 0.3$ keV), (2) moderate line broadening (HWHM ≈ 264 km s^{-1}) that is a factor of ∼4 below the terminal wind speed of σ Ori, (3) no significant mean line centroid shifts relative to laboratory values, (4) strong resonance and intercombination lines and very faint (formally undetected) forbidden lines with low f/i flux ratios, indicative of strong UV field excitation effects, and (5) Mg XI line formation within a few radii of the star ($r \lesssim 1.8R_*$).

5. INTERPRETATION OF THE X-RAY EMISSION FROM σ Ori AB

5.1. *Radiative Wind Shocks*

The temperature of the cool plasma that dominates the X-ray emission of σ Ori AB is in good agreement with model predictions

for shocks distributed in a radiatively driven stellar wind. Numerical radiation hydrodynamics simulations of shocks in radiatively driven winds give typical shock jumps $\Delta V = 500$–1000 km s^{-1} and postshock temperatures in the range $\sim$1–10 MK (Owocki et al. 1988). This range can easily accommodate σ Ori AB, whose emission measure–weighted temperature from the best-fit 2T APEC model is $T \sim 3.5$ MK.

The predicted postshock X-ray temperature corresponding to a shock jump velocity ΔV is $T_X = 1.4 \times 10^5 (\Delta V/100 \text{ km s}^{-1})^2$ K (Krolik & Raymond 1985). For σ Ori AB we have $T \sim 3.5 \times 10^6$ K ($kT = 0.3$ keV) so the required shock jump is $\Delta V \approx 500$ km s^{-1}, or about half the terminal wind speed.

Also, the emission measure (EM) in the wind is sufficient to account for the observed X-ray emission measure. The wind emission measure outside a given radius r_o is $\text{EM}_{\text{wind}}(r > r_o) = \int_{r_o}^{\infty} n_e n_{\text{H}} 4\pi r^2 \, dr$, where n_e and n_{H} are the electron and hydrogen number densities, respectively. Using the mass-loss parameters for σ Ori AB in Table 1 and assuming a solar-abundance constant-velocity wind with $v(r) = v_\infty$, we have $\text{EM}_{\text{wind}}(r > r_o) = 5.5 \times 10^{55}/r_o$ cm^{-3}, where r_o is in units of $R_* = 9\,R_\odot$. By comparison, the total X-ray emission measure determined from the best-fit 2T APEC model is $\text{EM}_X = 1.8 \times 10^{54}$ cm^{-3}. To compute this value, we have converted the normalization factors (norm) for both temperature components in Table 3 to equivalent emission measures and summed them, using the conversion $\text{EM} = 10^{14} 4\pi d_{\text{cm}}^2 (\text{norm})$, where d_{cm} is the stellar distance in cm. Adopting $r_o = 1.5$ as a representative example gives an inferred ratio of X-ray EM to wind EM of $\approx$5%. Thus, the emission measure of the X-ray–emitting plasma relative to that of the wind is low.

The grating spectra provide clues that a significant fraction of the X-ray emission originates close to the star in the region where the wind is still accelerating. The relatively narrow lines and absence of any significant centroid shifts are good evidence that the bulk of the X-ray plasma is slowly moving and does not form at large radii where the wind has reached terminal speed. Also, the very weak (formally undetected) forbidden lines in He-like triplets imply line formation close to the star. As already noted, the most stringent constraint on the location of the X-ray–emitting plasma comes from the Mg XI triplet, for which we infer an upper limit on the line formation radius $r < 1.8R_*$ (Fig. 22). Assuming a standard wind acceleration law $v(r) = v_\infty [1 - (R_*/r)]^\beta$ and $v_\infty = 1060$ km s^{-1} (Table 1), the above radius is within the acceleration zone for typical hot star wind values $\beta \approx 0.5$–1.0. A recent analysis of He-like triplet line ratios in O stars by Leutenegger et al. (2006) concludes that minimum line formation radii are typically $1.25 < r/R_* < 1.67$ and that these small radii do not preclude the formation of strong shocks.

A key question that remains to be answered is whether numerical simulations of the line-driven instability mechanism can reproduce the narrow line widths observed for σ Ori AB and some other late O and early B stars. As already noted (§ 4.2), the line widths observed for σ Ori AB have HWHM values equivalent to about one-fourth v_∞. But larger widths would be in better accord with numerical simulations, which tend to show shock onset radii of about $1.5R_*$ and velocities of shock-heated material that are an appreciable fraction of v_∞ (e.g., Feldmeier et al. 1997b; Runacres & Owocki 2002). Even so, it should be kept in mind that predicted line properties from simulations are sensitive to assumptions about wind properties and the wind velocity profile close to the star, which are uncertain for OB stars in general. A more detailed discussion of the issues related to line widths and profiles in nonmagnetic OB stars in the framework of radiative wind shock models will be presented in a future paper (D. Cohen et al. 2008, in preparation).

5.2. *Magnetically Confined Wind Shocks*

As already mentioned in the discussion of σ Ori E (§ 3.7.2), a sufficiently strong surface magnetic field can channel the wind of a hot star into two streams, producing X-ray emission from a magnetically confined wind shock near the magnetic equator. To our knowledge, there have been no published reports of a magnetic field detection on σ Ori AB. However, an upper limit on its line strength–weighted magnetic field of $B_l \leq -140$ ($\pm$260) G was obtained in the longer of the two observations reported by Landstreet (1982). Since the upper limit on B_l has a large uncertainty and this star is young with a rather uncertain age (Table 1 of Caballero 2007a), it could still retain a weak undetected fossil magnetic field. We thus briefly consider the MCWS mechanism.

Using the relation for the wind confinement parameter η (§ 3.7.2) and the adopted stellar parameters for σ Ori A (Table 1), the field strength for critical confinement ($\eta = 1$) is $B_{\text{eq}} \approx 70$ G. Thus, even a relatively weak field could perturb the wind of σ Ori A, but a field of this strength would be difficult to detect in a hot star.

Analytic expressions for the X-ray temperature and luminosity of a magnetically confined wind shock were derived by BM97a. The predicted temperature at the shock front is $T_{\text{shock}} = 1.13 \times 10^5 v_{100}^2$ K, where v_{100} is the preshock wind speed in units of 100 km s^{-1}. In order to reconcile the MCWS picture with the relatively cool emission at $T \sim 3.5$ MK observed for σ Ori AB, one would need to postulate a preshock wind speed of $v \sim 550$ km s^{-1}. This is about half the terminal wind speed and would require that the closed field lines exist only in the wind acceleration zone near the star ($r \lesssim 2R_*$ for values of β typical of hot star winds). Intuitively, this is what one would expect in the weak confinement regime.

The predicted X-ray luminosity from a magnetically confined wind shock in the BM97a model is $L_X \approx 2.6 \times 10^{30} B_{\text{kG}}^{0.4} \xi$ ergs s^{-1}. Here B_{kG} is the field strength in kG and ξ is a free parameter of the theory that depends on $\dot{M}$ and v_∞. For critical confinement ($B \sim 70$ G), this relation requires $\xi \sim 35$ to account for the observed L_X (Table 1). This value of ξ is within the (broad) range allowed by the theory and the adopted mass-loss parameters of σ Ori AB.

Based on the above comparisons, we conclude that the MCWS model could plausibly account for the observed X-ray properties of σ Ori AB if the magnetic field is weak and only able to close the field lines near the star. Detailed MCWS simulations would be needed to test this idea. The justification for invoking the MCWS model is not strong in the absence of a magnetic field detection or any documented Hα or UV wind line modulation.

5.3. *Colliding Wind Shocks*

The presence of a B0.5 V companion at a separation of 0.25″ from σ Ori A raises the possibility that X-rays could be produced in a colliding wind shock region between the two stars. However, the predicted maximum X-ray temperature for a colliding wind shock in the case of solar abundances is $kT_{\text{cw}} \approx 1.17 (v_{\perp,1000})^2$ keV, where $v_{\perp,1000}$ is the velocity of the wind component perpendicular to the shock interface in units of 1000 km s^{-1} (Stevens et al. 1992). Setting $v_\perp$ equal to the terminal wind speed of σ Ori AB gives $kT_{\text{cw}} \approx 1.3$ keV, much higher than observed.

Furthermore, wind momentum balance considerations predict that the shock contact discontinuity along the line of centers between the binary components will lie at least $\sim 1000 R_{\text{O star}}$ from σ Ori A. This equates to about half the distance between the A

and B components. To arrive at this estimate, we have assumed that the winds have reached terminal speeds and have used eq. [1] of Stevens et al. (1992), along with the mass-loss parameters in Table 1 and the assumed B0.5 V star wind parameters $\log \dot{M}_{\rm B\ star} \sim -7.4$ to -8.0 ($M_\odot$ yr^{-1}) and $v_{\infty,\rm B\ star} \sim 2000$ km s^{-1} (Abbott 1982; Cassinelli et al. 1994). X-ray formation at such large distances is ruled out by the weak or absent forbidden lines in He-like ions, which for Mg XI demonstrate that the bulk of the X-rays are formed within a few radii of the O star.

Based on the above estimates, a colliding wind origin for the X-rays seems very unlikely. However, before ruling out this mechanism, it is important to note that there have been several reports that σ Ori A is itself a double-lined spectroscopic binary (e.g., Bolton 1974; Morrell & Levato 1991), which if true would make σ Ori AB a triple system. This has also been mentioned by Caballero (2008) as a possible means of bringing the derived distance of σ Ori AB into better agreement with that of the cluster.

If the A component is indeed a spectroscopic binary, then the wind of the more massive primary could be shocking onto the wind of the spectroscopic companion. From above, the wind speed needed to produce the $kT \approx 0.3$ keV plasma detected by *Chandra* is $v_{\rm wind} \approx 500$ km s^{-1}. This would imply that the winds are shocking at subterminal speeds. For a $\beta = 1$ velocity law, this speed could be achieved at $r \approx 1.9R_*$, and for $\beta = 0.8$ the computed radius is $r \approx 1.6R_*$. Considering our imprecise knowledge of the wind velocity law close to the star, these values are compatible with the upper limit $r \leq 1.8R_*$ obtained from Mg XI line flux ratios (§ 4.4).

A close colliding wind system consisting of σ Ori A and a spectroscopic companion might resemble close spectroscopic binaries such as HD 150136. This massive O3 + O6 V SB2 system has a short-period 2.66 day orbit (Niemela & Gamen 2005). A sensitive *Chandra* HETG observation detected HD 150136, but the O3 + O6 V SB2 system could not be spatially resolved (Skinner et al. 2005). The X-ray spectrum of HD 150136 is soft with a characteristic temperature $kT \approx 0.3$ keV, remarkably similar to that detected here in σ Ori AB. Because of the close separation of the two components in HD 150136, the winds would be shocking at subterminal speeds and radiative cooling in the shock region is important (Skinner et al. 2005). Thus, the predicted temperature for a colliding wind shock is lower than for an equivalent adiabatic system at wide separation. If the analogy between the O3 + O6 V spectroscopic binary HD 150136 and σ Ori A is indeed relevant, then an early B star may be playing the role of the spectroscopic companion to σ Ori A (Caballero 2008).

If σ Ori A does have a spectroscopic companion, then orbitally modulated X-ray emission could be present if the X-rays form in a colliding wind shock. However, the presence of orbital X-ray modulation depends critically on the orbital eccentricity and inclination, for which no information is currently available. We see no clear evidence for X-ray modulation in the ~1 day *Chandra* light curve (Fig. 4). More specific information on the properties of the putative spectroscopic companion and its orbit would be needed to make further comparisons between colliding wind shock theory and the X-ray data.

5.4. *Coronal Models and Late-Type Companions*

The existence of a thin X-ray–emitting coronal zone at the base of the wind was invoked by Cassinelli & Olson (1979) to explain strong O VI, N V, and C IV lines in some OB supergiants and Of stars. Waldron & Cassinelli (2001) have also proposed a composite model involving both wind shocks and confinement of dense plasma in magnetic loops close to the star to explain the broad emission lines detected in the O9.7 Ib star ζ Ori, but Cohen et al. (2006) arrive at a different interpretation that does not invoke magnetic confinement. Magnetic loop confinement close to the star strongly resembles coronal models for late-type stars.

However, the coronal model has not gained wide acceptance due to the lack of a solid theoretical basis for explaining how strong outer convection zones would be produced in hot stars. Such convection zones are thought to be essential for generating self-sustained magnetic fields in the Sun and other late-type stars. Even so, the detection of strong ~kG magnetic fields in some very young O-type stars such as θ^1 Ori C (Donati et al. 2002) does justify a brief examination of the possibility of coronal emission, from either σ Ori AB or an unseen late-type companion.

Because of the young age of σ Ori AB (~3 Myr), a coeval unseen late-type companion would likely be a T Tauri star and thus a potential X-ray emitter. However, adaptive optics *H*-band images with FWHM $\approx 0.2''$–$0.4''$ (Caballero 2005) have only detected IRS 1, which at a separation of $\approx 3''$ is also revealed by *Chandra*. The best adaptive optics resolution of FWHM $\approx 0.2''$ probes down to a linear separation of ~70 AU, so any as yet undetected T Tauri star would presumably lie very close to σ Ori A.

Most T Tauri stars detected in the deep *Chandra* Orion COUP survey show a hot X-ray component at $kT > 1$ keV (Preibisch et al. 2005). We do not detect such a component in the X-ray spectrum of σ Ori AB, so the observed temperature structure provides no hint for a T Tauri companion. Impulsive X-ray flaring or moderate amplitude variability on short timescales is often (but not always) detected in T Tauri stars, but no such variability has so far been detected in σ Ori AB. Finally, at the spectral resolution of *Chandra*'s HETG, emission lines of coronal late-type stars such as Capella (Ness et al. 2003) and of T Tauri stars such as SU Aur (Smith et al. 2005) and HDE 245059 (Baldovin Saavedra et al. 2007) show narrow lines with no broadening beyond thermal widths, in contrast to the broadened lines detected here in σ Ori AB. Thus, we find no strong reason to invoke a coronal interpretation for the X-ray emission of σ Ori AB.

6. CONCLUSIONS

The main conclusions of this study are the following:

1. *Chandra* detected 42 X-ray sources on the ACIS-S3 CCD in the central region of the σ Ori cluster. Three are known high-mass OB stars, and the remainder have X-ray and near-IR properties consistent with magnetically active K or M stars. Nineteen of the X-ray sources have K or M spectral types determined from previous studies, and about half of these show near-IR excesses based on 2MASS colors.

2. The X-ray emission associated with IRS 1 is variable and shows a high-temperature ($kT \gtrsim 1$ keV) component. Its X-ray properties and elongated mid-IR morphology suggest that it is a low-mass magnetically active T Tauri star whose disk/envelope is being photoevaporated by σ Ori AB.

3. The X-ray emission of σ Ori E is variable and a hard component ($kT \approx 2.6$ keV) is detected, as typical of magnetically active stars. Its ratio L_X/L_* is unusually high for a B2 V star assuming the nominal distance of 640 pc, suggesting that it could lie closer. Numerical magnetosphere models based on the magnetically confined wind picture predict hot plasma at temperatures similar to (but slightly higher than) observed and can also explain many aspects of the variability of this star (Townsend et al. 2005, 2007). Future numerical models offer the potential to provide estimates of X-ray luminosity and X-ray absorption that can be directly compared with observations.

4. The X-ray emission of the OB binary system σ Ori AB is exceptional, being the most luminous X-ray source in the field and the softest. Its low X-ray temperature ($kT \approx 0.3$ keV) and moderately broadened emission lines (HWHM ≈ 264 km s^{-1}) clearly argue against a coronal interpretation and point to a shock origin. Overall, its X-ray properties are quite similar to some other late O and early B stars for which X-ray grating spectra show relatively cool plasma and slightly broadened unshifted symmetric emission lines.

5. Radiative wind shock predictions for an optically thin wind are consistent with the cool plasma and symmetric unshifted emission lines of σ Ori AB. However, the rather narrow line widths and low f/i ratios imply X-ray formation in slowly moving plasma in the wind acceleration zone close to the star. It remains to be seen whether future numerical simulations of the line-driven instability mechanism can reproduce the narrow lines.

6. Other possible emission mechanisms for σ Ori AB that are not yet totally ruled out but remain speculative are (*a*) a magnetically confined wind shock in the weak-field limit and (*b*) a subterminal speed colliding wind system if σ Ori A does have a spectroscopic companion. The MCWS scenario lacks solid observational support in the absence of any evidence for a magnetic field in σ Ori AB. More complete information about the properties of the putative spectroscopic companion and its orbit will be needed to make meaningful comparisons of colliding wind theory with observations.

We thank Victoria Swisher for assistance with data analysis and Stephen Drake for providing information on VLA observations of σ Ori. This research was supported by grants GO5-6009X (SAO) and NNG05GE69G (NASA GSFC).

REFERENCES

Abbott, D. C. 1982, ApJ, 259, 282
Anders, E., & Grevesse, N. 1989, Geochim. Cosmochim. Acta, 53, 197
Babel, J., & Montmerle, T. 1997a, A&A, 323, 121 (BM97a)
———. 1997b, ApJ, 485, L29
Baldovin Saavedra, C., Audard, M., Duchêne, G., Güdel, M., Skinner, S. L., & Paerels, F. B. S. 2007, BAAS, 39, 851
Berghöfer, T. W., & Schmitt, J. H. M. M. 1994, A&A, 290, 435
Berghöfer, T. W., Schmitt, J. H. M. M., & Cassinelli, J. P. 1996, A&AS, 118, 481
Bessell, M. A., & Brett, J. M. 1988, PASP, 100, 1134
Blumenthal, G. R., Drake, G. W. F., & Tucker, W. H. 1972, ApJ, 172, 205 (BDT72)
Bolton, C. T. 1974, ApJ, 192, L7
Borra, E. F., & Landstreet, J. D. 1979, ApJ, 228, 809
Brandt, W. N., et al. 2001, AJ, 122, 2810
Caballero, J. A. 2005, Astron. Nachr., 326, 1007
———. 2007a, A&A, 466, 917
———. 2007b, Astron. Nachr., 328, 917
———. 2008, MNRAS, 383, 750
Cassinelli, J. P., Cohen, D. H., Macfarlane, J. J., Sanders, W. T., & Welsh, B. Y. 1994, ApJ, 421, 705
Cassinelli, J. P., Miller, N. A., Waldron, W. A., Macfarlane, J. J., & Cohen, D. H. 2001, ApJ, 554, L55
Cassinelli, J. P., & Olson, G. L. 1979, ApJ, 229, 304
Cohen, D. H., Cassinelli, J. P., & Macfarlane, J. J. 1997, ApJ, 487, 867
Cohen, D. H., Cooper, R. G., Macfarlane, J. J., Owocki, S. P., Cassinelli, J. P., & Wang, P. 1996, ApJ, 460, 506
Cohen, D. H., de Messières, G. E., Macfarlane, J. J., Miller, N. A., Cassinelli, J. P., Owocki, S. P., & Liedahl, D. A. 2003, ApJ, 586, 495
Cohen, D. H., Kuhn, M. A., Gagné, M., Jensen, E. L. N., & Miller, N. A. 2008, MNRAS, 386, 1855
Cohen, D. H., Leutenegger, M. A., Grizzard, K. T., Reed, C. L., Kramer, R. H., & Owocki, S. P. 2006, MNRAS, 368, 1905
Cowie, L. L., Garmire, G. P., Bautz, M. W., Barger, A. J., Brandt, W. N., & Hornschemeier, A. E. 2002, ApJ, 566, L5
Donati, J.-F., Babel, J., Harries, T. J., Howarth, I. D., Petit, P., & Semel, M. 2002, MNRAS, 333, 55
Drake, S. A. 1990, AJ, 100, 572
Edwards, T. W. 1976, AJ, 81, 245
Favata, F., et al. 2005, ApJS, 160, 469
Feldmeier, A., Kudritzki, R.-P., Palsa, R., Pauldrach, A. W. A., & Puls, J. 1997a, A&A, 320, 899
Feldmeier, A., Puls, J., & Pauldrach, A. W. A. 1997b, A&A, 322, 878
Flaccomio, E., et al. 2005, ApJS, 160, 450
Franciosini, E., Pallavicini, R., & Sanz-Forcada, J. 2006, A&A, 446, 501 (FPS06)
Gabriel, A. H., & Jordan, C. 1969, MNRAS, 145, 241
Gagné, M., et al. 2005, ApJ, 628, 986
Gatti, T., Natta, A., Randich, S., Testi, L., & Sacco, G. 2008, A&A, 481, 423
Getman, K. V., et al. 2005, ApJS, 160, 319
Gorenstein, P. 1975, ApJ, 198, 95
Groote, D., & Hunger, K. 1997, A&A, 319, 250
Groote, D., & Schmitt, J. H. M. M. 2004, A&A, 418, 235
Hernández, J., et al. 2007, ApJ, 662, 1067
Howarth, I. D., & Prinja, R. K. 1989, ApJS, 69, 527
Hunger, K., Heber, U., & Groote, D. 1989, A&A, 224, 57
Ignace, R., Oskinova, L. M., & Foullon, C. 2000, MNRAS, 318, 214
Jeffries, R. D. 2007, MNRAS, 376, 1109
Kahn, S. M., et al. 2001, A&A, 365, L312
Kenyon, S. J., & Hartmann, L. 1995, ApJS, 101, 117
Kramer, R. H., Cohen, D. H., & Owocki, S. P. 2003, ApJ, 592, 532
Krolik, J. H., & Raymond, J. C. 1985, ApJ, 298, 660
Landstreet, J. D. 1982, ApJ, 258, 639
Landstreet, J. D., & Borra, E. F. 1978, ApJ, 224, L5
Lanz, T., & Hubeny, I. 2007, ApJS, 169, 83
Lee, T. A. 1968, ApJ, 152, 913
Leutenegger, M. A., Paerels, F. B. S., Kahn, S. M., & Cohen, D. C. 2006, ApJ, 650, 1096
Lucy, L. B. 1982, ApJ, 255, 286
Lucy, L. B., & White, R. L. 1980, ApJ, 241, 300
Macfarlane, J. J., Cassinelli, J. P., Welsh, B. Y., Vedder, P. W., Vallerga, J. V., & Waldron, W. L. 1991, ApJ, 380, 564
Mason, B. D., Gies, D. R., Hartkopf, W. I., Bagnuolo, W. G., Brummelaar, T. T., & McAlisster, H. A. 1998, AJ, 115, 821
Mayne, N. J., & Naylor, T. 2008, MNRAS, 386, 261
Mayne, N. J., Naylor, T., Littlefair, S. P., Saunders, E. S., & Jeffries, R. D. 2007, MNRAS, 375, 1220
Menten, K. M., Reid, M. J., Forbrich, J., & Brunthaler, A. 2007, A&A, 474, 515
Miller, N. A., Cassinelli, J. P., Waldron, W. L., Macfarlane, J. J., & Cohen, D. H. 2002, ApJ, 577, 951
Morrell, N., & Levato, H. 1991, ApJS, 75, 965
Nakajima, R. 1985, Ap&SS, 116, 285
Ness, J.-U., Brickhouse, N. S., Drake, J. J., & Huenemoerder, D. P. 2003, ApJ, 598, 1277
Niemela, V. S., & Gamen, R. C. 2005, MNRAS, 356, 974
Oliveira, J. M., Jeffries, R. D., van Loon, J. Th., & Rushton, M. T. 2006, MNRAS, 369, 272
Owocki, S. P., Castor, J. I., & Rybicki, G. B. 1988, ApJ, 335, 914
Owocki, S. P., & Cohen, D. H. 2001, ApJ, 559, 1108
Pauldrach, A. W. A., Kudritzki, R. P., Puls, J., Butler, K., & Hunsinger, J. 1994, A&A, 283, 525
Perryman, M. A. C., et al. 1997, A&A, 323, L49
Porquet, D., Mewe, R., Dubau, J., Raassen, A. J. J., & Kaastra, J. S. 2001, A&A, 376, 1113
Pradhan, A. K. 1982, ApJ, 263, 477
Preibisch, T., & Feigelson, E. D. 2005, ApJS, 160, 390
Preibisch, T., et al. 2005, ApJS, 160, 401
Press, W. H., Teukolsky, S. A., Vetterling, W. T., & Flannery, B. P. 1992, Numerical Recipes in FORTRAN: The Art of Scientific Computing (2nd ed.; New York: Cambridge Univ. Press), 617
Reiners, A., Stahl, O., Wolf, B., Kaufer, A., & Rivinius, T. 2000, A&A, 363, 585
Rieke, G. H., & Lebofsky, M. J. 1985, ApJ, 288, 618
Runacres, M. C., & Owocki, S. P. 2002, A&A, 381, 1015
Sandstrom, K. M., Peek, J. E. G., Bower, G. C., Bolatto, A. D., & Plambeck, R. L. 2007, ApJ, 667, 1161
Sanz-Forcada, J., Franciosini, E., & Pallavicini, R. 2004, A&A, 421, 715
Savage, B. D., Massa, D., Meade, M., & Wesselius, P. R. 1985, ApJS, 59, 397
Schulz, N. S., Canizares, C. R., Huenemoerder, D., & Lee, J. C. 2000, ApJ, 545, L135
Sherry, W. H., Walter, F. M., & Wolk, S. J. 2004, AJ, 128, 2316 (S04)
Skinner, S. L., Brown, A., & Stewart, R. T. 1993, ApJS, 87, 217

Skinner, S. L., Zhekov, S. A., Palla, F., & Barbosa, C. L. D. R. 2005, MNRAS, 361, 191
Smith, K., Audard, M., Güdel, M., Skinner, S., & Pallavicini, R. 2005, in Proc. 13th Cambridge Workshop on Cool Stars, Stellar Systems, and the Sun, ed. F. Favata et al. (ESA SP-560; Noordwijk: ESA), 971
Smith, R. K., Brickhouse, N. S., Liedahl, D. A., & Raymond, J. C. 2001, ApJ, 556, L91
Stelzer, B., et al. 2005, ApJS, 160, 557
Stevens, I. R., Blondin, J. M., & Pollock, A. M. T. 1992, ApJ, 386, 265
Telleschi, A., Güdel, M., Briggs, K. R., Audard, M., & Palla, F. 2007, A&A, 468, 425
Townsend, R. H. D., Owocki, S. P., & Groote, D. 2005, ApJ, 630, L81
Townsend, R. H. D., Owocki, S. P., & ud-Doula, A. 2007, MNRAS, 382, 139
ud-Doula, A., & Owocki, S. P. 2002, ApJ, 576, 413
van Loon, J. Th., & Oliveira, J. M. 2003, A&A, 405, L33
Vogt, N. 1976, A&A, 53, 9
Waldron, W., & Cassinelli, J. P. 2001, ApJ, 548, L45
Waldron, W., Corcoran, M. F., Drake, S. A., & Smale, A. P. 1998, ApJS, 118, 217
Walter, F. M., Wolk, S. J., Freyberg, M., & Schmitt, J. H. M. M. 1997, Mem. Soc. Astron. Italiana, 68, 1081
Wolk, N. R., Wolk, S. J., Walter, F. M., & Sherry, W. H. 2006, in Protostars and Planets V, ed. B. Reipurth, D. Jewitt, & K. Keil (Tucson: Univ. Arizona Press), 8425
Zapatero Osorio, M. R., et al. 2002, A&A, 384, 937